Investigations of the Münster dual phase xenon time projection chamber

BACHELOR THESIS

Henning Schulze Eißing

Westfälische Wilhelms-Universität Münster
Institut für Kernphysik
AG Weinheimer

Themensteller: Prof. Dr. C. Weinheimer
Zweitgutachter: Prof. Dr. A. Kappes

Münster, Oktober 2017

Eidesstattliche Erklärung

Hiermit versichere ich, dass die vorliegende Arbeit über *Investigations of the Münster dual phase xenon time projection chamber* selbstständig verfasst worden ist, dass keine anderen Quellen und Hilfsmittel als die angegebenen benutzt worden sind und dass die Stellen der Arbeit, die anderen Werken - auch elektronischen Medien - dem Wortlaut oder Sinn nach entnommen wurden, auf jeden Fall unter Angabe der Quelle als Entlehnung kenntlich gemacht worden sind.

Münster, 30. Oktober 2017

Vorname, Nachname

Ich erkläre mich mit einem Abgleich der Arbeit mit anderen Texten zwecks Auffindung von Übereinstimmungen sowie mit einer zu diesem Zweck vorzunehmenden Speicherung der Arbeit in eine Datenbank einverstanden.

Münster, 30. Oktober 2017

Vorname, Nachname

Contents

1 Introduction

A dual phase time projection chamber (TPC) is a particle detector which is suitable for rare event seaches due to its scalability and the possibility to reject background signals. One application is the direct detection of dark matter which was postulated at the beginning of the 1930s but has not yet been directly detected.

The XENON Dark Matter Project located at the Laboratori Nazionali del Gran Sasso (LNGS) aims at the direct detection of dark matter. It utilizes a dual phase time projection chamber to search for nuclear recoil signals of Weakly Interacting Massive Particles (WIMPs) by scattering off xenon nuclei. The current stage XENON1T is the world's most sensitive experiment for direct dark matter detection.

In 2011 a smaller version of such a detector was built in Münster in order to be able to perform different investigations which include studies on electron lifetime, which provide a conclusion on the purity of the target material xenon as well as different calibration sources. Additionally, the detector was conceived for teaching purposes.

The objective of this bachelor thesis is to achieve two calibrations which are needed to perform further investigations with the Münster TPC. This concerns the gain calibration of the photomultipliers and the determination of the optimal liquid level. In the first chapter the working principle of a dual phase time projection chamber is explained. Then the method of determining the photomultiplier gain is described and the gain for each PMT is determined subsequently. The third chapter is dedicated to the determination of the optimal liquid level. These results are applied in order to identify signals of the used calibration source in the recorded data. In the end the results will be summarized and discussed. Furthermore, an outlook on future measurements with the Münster TPC will be given.

2 Dual phase time projection chamber

A dual phase time projection chamber is a detector that contains a sensitive gas and liquid volume to determine the position and deposited energy of a particle scattering in the target material [1]. For this purpose, the scintillation light and charge carriers, created by interactions are measured. Due to their design, TPCs are suitable for rare event searches like direct dark matter detection. In this section, the functional principle of a TPC is explained followed by a discussion, why xenon is suitable as a detector medium. Finally the setup of the TPC built in Münster and a calibration source will be presented.

2.1 Working principle

Within a TPC an incoming particle can interact with the atomic shell or with the nucleus of the detector medium. These reactions are called electronic recoils and nuclear recoils, respectively. Both interaction types produce scintillation photons and ionization charges. Photomultiplier tubes (PMTs) are mounted on the top and bottom of the detector to measure light signals in the detector. The prompt scintillation signals, called S1, within the liquid phase are mostly seen on the bottom PMTs due to total internal reflection on the liquid gas interface. The electrons, released by ionization, are drifted in the direction of the gas phase by an external electric field. This drift field E_{drift} is created by two meshes on different electric potential. The bottom mesh is set to a negative potential (cathode), while the mesh at the liquid-gas interface, the gate mesh, is set to ground potential. A second field called extraction field $E_{extraction}$ between the gate and the mesh on top of the TPC which is set to positive potential (anode), extracts the electrons from the liquid phase into the gas phase. There, they are accelerated by the anode and cause a second scintillation signal by the interaction with the xenon atoms in the gas phase. This delayed scintillation signal is called S2 and is mostly seen on the top PMTs. The signal strength of the S2 is proportional to the number of extracted electrons and significantly higher than the strength of the S1 signal.

As mentioned above, it is possible to determine the position of an interaction in the detector volume: The time difference between the S1 and S2 signal, in which the ionization electrons move at a constant speed towards the liquid-gas interface is used to determine the depth

(z-coordinate) of the interaction. The x- and y-coordinate can be determined by the hit pattern of the S2 signal on the top PMT-array.

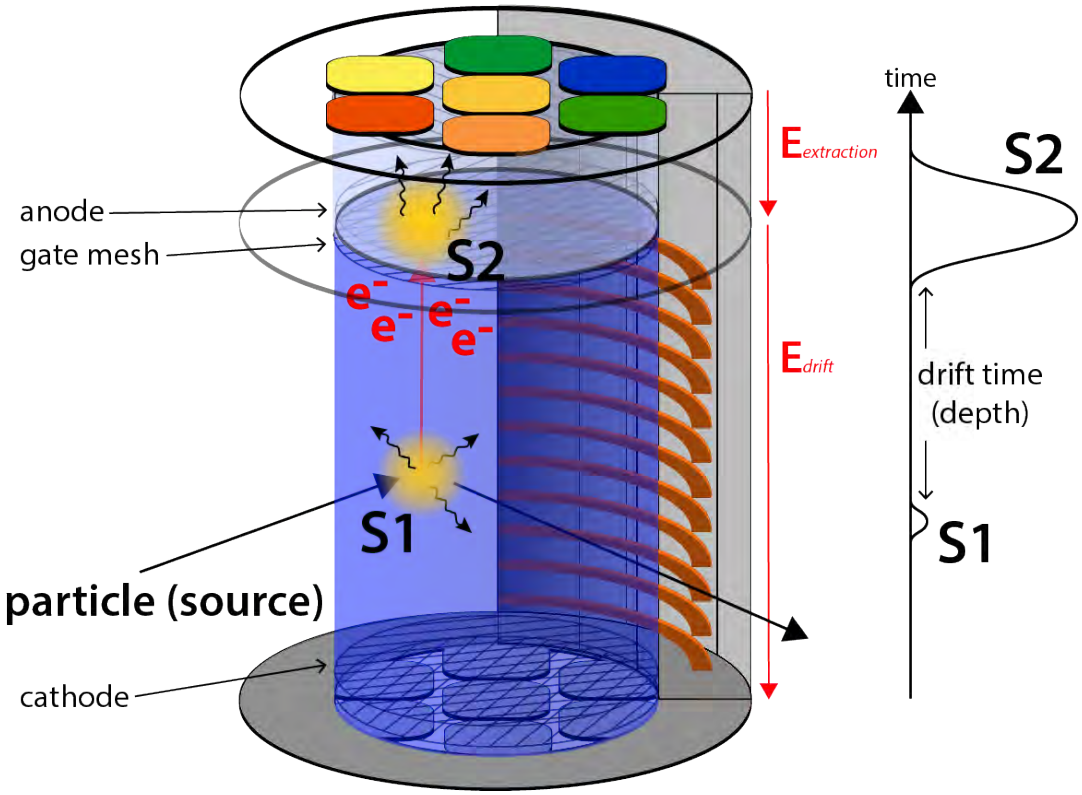

Figure 2.1: Schematic of the Münster TPC [2]. The xenon ist presented in blue. The electric fields are shaped by the copper rings. The PMTs are marked with different colors to illustrate the recorded light intensities.

2.1.1 Xenon as detector medium

Xenon offers some advantages over other detector media that qualify it specifically for the usage in a dual phase TPC. Due to its high atomic number of $Z = 54$ and its high density of $\sim 3\,\mathrm{g/cm^3}$ for liquid xenon it has a high stopping power for penetrating α, β and γ radiation which represent the major backgrounds for rare event searches. Using this self-shielding property and the position reconstruction of the dual phase TPC, it is possible to define a sensitive volume in the center of a large TPC which is used as target volume for the dark matter search.

For liquid xenon the average energy required to produce an electron ion pair of $W_{e,\,Xe} = (15.6 \pm 0.3)\,\mathrm{eV}$ is significantly lower than for liquid argon with

$W_{e,\,Ar} = (23.6 \pm 0.3)\,eV$. Furthermore, the average needed energy[1] of $W_{ph,\,Xe} = 21.6\,eV$ to produce a scintillation photon in liquid xenon is also lower than the energy of $W_{ph,\,Ar} = 24.4\,eV$ needed in liquid argon [4]. Since a lower minimum energy transfer is necessary to generate a signal, a lower energy threshold can be achieved with xenon.

The scintillation process of xenon is based on the de-excitation of an excited xenon dimer (Xe_2^*) into the ground state by the emission of a photon. There are two ways of creating these dimers [4]. For the first reaction an excited xenon atom is needed, which is created by a scattering process with an incoming particle. The excited xenon atom forms a xenon dimer Xe_2^* with a non excited atom:

$$\begin{aligned} Xe^* + Xe + Xe &\rightarrow Xe_2^* + Xe \\ Xe_2^* &\rightarrow 2Xe + h\nu. \end{aligned} \tag{2.1}$$

The xenon dimer returns to its ground state by photon emission.

The second process starts with a xenon ion. Together with an additional xenon atom, this ion forms an ionized dimer which disintegrates into an excited atom and an atom in the ground state by absorbing an electron. The excited xenon atom changes into a lower excited state by a radiationless transition. Thereafter, the processes described in equation (2.1) also takes place here:

$$\begin{aligned} Xe^+Xe &\rightarrow Xe_2^+ \\ Xe_2^+ + e^- &\rightarrow Xe^{**} + Xe \\ Xe^{**} &\rightarrow Xe^* + \text{heat} \\ Xe^* + Xe + Xe &\rightarrow Xe_2^* + Xe \\ Xe_2^* &\rightarrow 2Xe + h\nu. \end{aligned} \tag{2.2}$$

In liquid xenon, scintillation photons have a wavelength of 177.6 nm [4]. Due to the fact, that the scintillation photons are emitted from dimers, xenon is transparent for its own scintillation light.

2.2 Münster TPC

The *Münster dual phase time projection chamber* uses a cylindrical detector volume filled with 2.56 kg liquid and gaseous xenon [5] as shown in the schematic in figure 2.1. In total,

[1] Usually an average value of (13.7 ± 0.2) eV from the ionization and scintillations W-values is used here for liquid xenon [3].

there are 14 Hamamatsu R8520-06-AL photomultiplier tubes placed at the top and bottom of the detector in 2-3-2 arrays. Each PMT has a diagonal of one inch and was chosen due to its low radioactivity. The inner vessel has a height of 170 mm and a diameter of 80 mm and is made of polytetrafluoroethylene (PTFE), more commonly known as Teflon® which has a high reflectivity for 178 nm photons [6]. The electric fields are caused by three meshes and shaped by copper rings. The drift field has a strength of about 500 $\frac{\mathrm{V}}{\mathrm{cm}}$ so that the free electrons have a drift velocity of 2 mm/μs [7]. The extraction field has a strength of 5 $\frac{\mathrm{kV}}{\mathrm{cm}}$.

2.3 ^{83m}Kr as a calibration source

Due to the self-shielding of the liquid xenon, it is difficult to use an external low energy calibration source. It is therefore preferable to use a source directly injected into the liquid xenon. However, the half-life of this radioactive source must be short enough to prevent a long-term contamination of the detector. ^{83m}Kr is suitable for this kind of application [8].

^{83}Rb decays to ^{83m}Kr by electron capture with a half-life of 86.2 days as shown in the simplified decay scheme in Figure 2.2. The isomer ^{83m}Kr undergoes two highly converted transitions into ^{83}Kr with half-lifes of 1.83 h and 154 ns respectively.

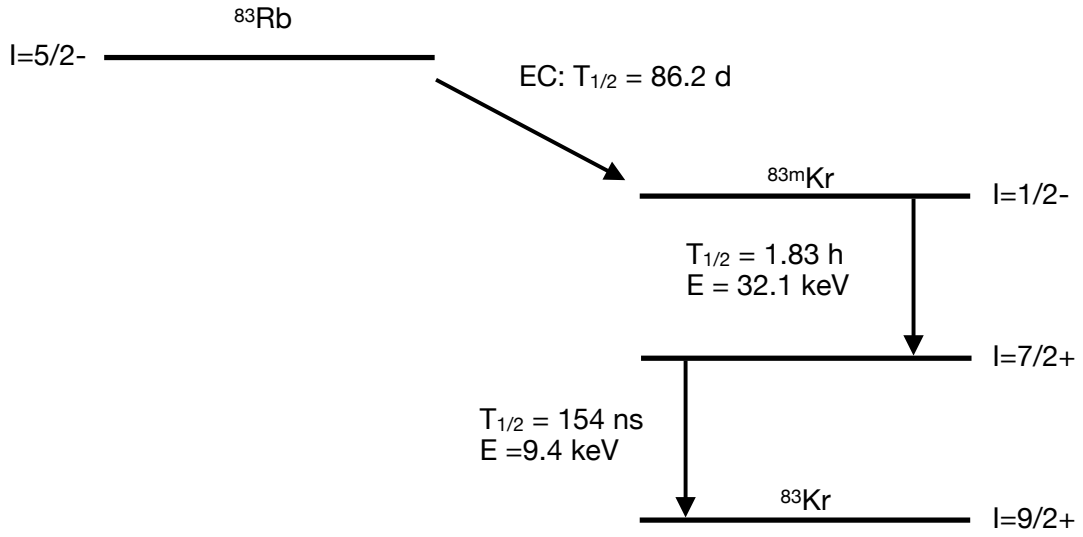

Figure 2.2: Scheme of ^{83}Rb and ^{83m}Kr decay. Rubidium decays to ^{83m}Kr via electron capture which then decays to ^{83}Kr via an intermediate step.

The gaseous ^{83m}Kr emitted by a solid rubidium source can be introduced directly into the gas circulation of the system to ensure homogeneous distribution inside the detector. This can only be achieved because the half-life of the ^{83m}Kr decay is sufficient to ensure a mixing of the ^{83m}Kr in the detector before it decays.

3 Photomultiplier gain

Since photomultipliers are used to measure the S1 and S2 signals in the TPC, it is necessary to deduce the energy deposited in the detector from the voltage signal of the PMTs. In this chapter, the functionality of a PMT will be explained first, subsequently the charge amplification of the individual PMTs will be determined.

3.1 Photomultiplier tube

Photomultiplier tubes are detectors for photons in the range of ultraviolet, visible and near infrared electromagnetic radiation. Due to their design, PMTs are able to generate measurable signals even for a single photon. A PMT consists of a cathode, several dynodes and an anode connected by a voltage divider circuit in an evacuated tube as shown in Figure 3.1. When a photon hits the cathode of the PMT through the input window, it can free an

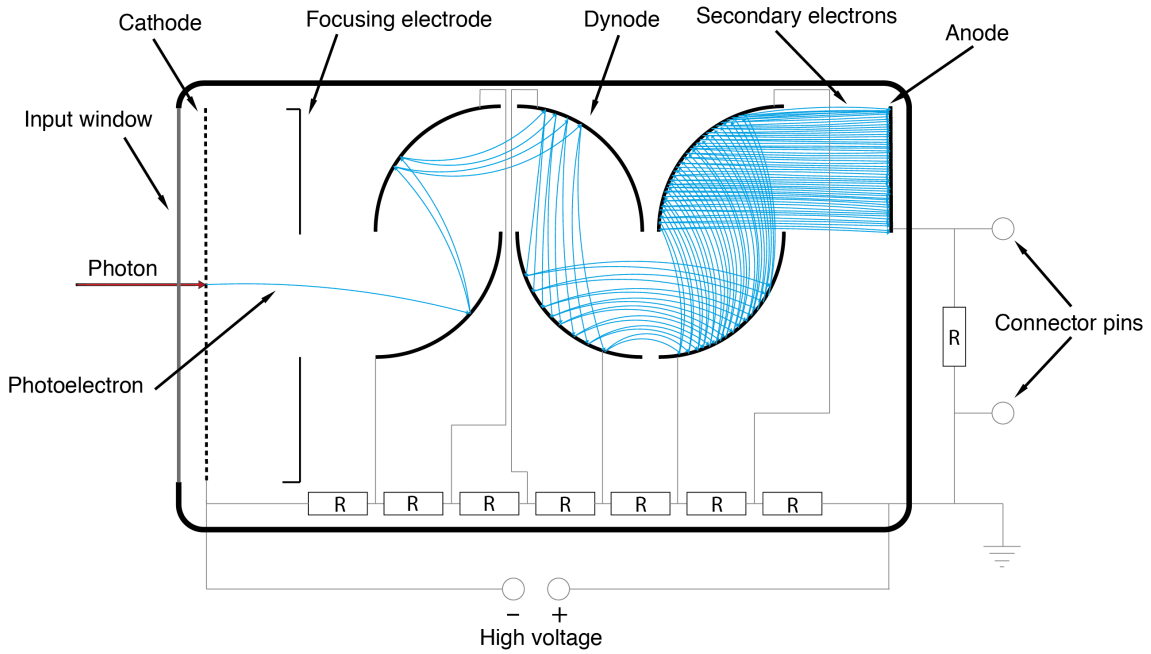

Figure 3.1: Schematic of a photomultiplier tube. A Photon frees a photoelectron from the Cathode. The number of secondary electrons increases from dynode to dynode [9].

electron by the external photoelectric effect. These so-called photoelectrons (pe) are emitted into the surrounding vacuum of the tube and accelerated by a focussing electrode towards the first dynode. The electric potential increases from dynode to dynode. When photoelectrons hit the dynode surface, secondary electrons are emitted for every initial photoelectron. As before, the electrons are accelerated by the potential difference in direction of the next dynode. This sequence is repeated for each dynode. Finally, all secondary electrons are collected by the anode which passes the charges to an external circuit. In order to use a PMT in a proper way, it is important to know the collected charge, if only one photon hits the cathode. This charge depends on the quantum efficiency η of the cathode and the charge amplification of the dynodes μ called *gain*. The quantum efficiency is defined as the ratio of emitted photoelectrons N_{pe} and photons hitting the cathode N_{p}:

$$\eta = \frac{N_{\mathrm{pe}}}{N_{\mathrm{p}}}. \tag{3.1}$$

The secondary emission ratio δ_n of the i-th dynode is defined as

$$\delta_i = \frac{N_{di}}{N_{d(i-1)}}, \tag{3.2}$$

where N_{di} is the number of secondary electrons emitted by dynode i and $N_{d(i-1)}$ is the number of secondary electrons emitted by dynode $(i-1)$. The number of electrons collected by the anode is given by

$$N_{\mathrm{A}} = N_{\mathrm{pe}} \cdot \alpha \cdot \prod_{i}^{n} \delta_i = N_{\mathrm{pe}} \cdot \mu. \tag{3.3}$$

In this equation, n is the number of dynodes and α is the collection efficiency. The secondary emission ratio can be calculated with the interstage voltage E [9]:

$$\delta = a \cdot E^k. \tag{3.4}$$

Here, a is a constant and k is determined by the dynode structure and material. For a PMT with an equally distributed voltage divider, where the potential difference between the dynodes is constant, with a collection efficiency of $\alpha = 1$ and a power supply voltage V, the gain can be written as

$$\mu = (a \cdot E^k)^n = a^n \cdot \left(\frac{V}{n+1}\right)^{kn} = A \cdot V^{kn}. \tag{3.5}$$

3.2 Measurement of the gain with a UV-LED

As mentioned above, it is essential to know the charge amplifications and quantum efficiencies of the used PMTs in order to determine the energy deposited in the detector. An UV-LED operated at a low intensity can be used to determine the charge amplification for each PMT [10]. The light from the pulsed LED is directed through a glass fiber into the TPC. If only a single electron is emitted at the PMT cathode, the charge given off by the PMT corresponds to the gain. If two electrons are emitted, the charge collected by the anode corresponds to twice the gain. The incidence of these events can be varied by the trigger settings and the LED intensity, such that in about 95% of the cases only one electron is emitted. In about 4.9% of the cases two electrons are emitted. These probabilities and the probabilities of multi electron events are described by a Poisson distribution in all cases:

$$P_\lambda(k) = \frac{\lambda^k}{k!} e^{-\lambda}. \tag{3.6}$$

Here, P is the probability for the number k of emitted photoelectrons and λ is the rate of these events.

The UV-LED is powered periodically by a pulse generator at a frequency of 100 kHz and a trigger signal with a frequency of 1 kHz is transmitted to the measurement electronics and data recording is started. In figure 3.2, the number of analog digital converter (ADC) counts is plotted against the sample number in an event. One sample corresponds to a period of 10 ns, one event has 512 samples each. The trigger is marked in red. When electrons are collected a voltage drop can be registered at the anode. This is translated to a drop in ADC counts which is proportional to the PMT gain.

The program *wfview* created in Münster calculates the collected charge at the PMT anode in the green marked window according to

$$Q = \int_{t_i}^{t_f} \frac{U(t)}{R} dt \tag{3.7}$$

where t_i is the initial time and t_f is the final time of the integration window. U is the time dependent voltage and R the electrical resistance of the flash-analog-to-digital-converter input channel.

Due to the fact that the data acquisition uses discrete time samples with a sample size of $\Delta s = 10\,\text{ns}$ the integral can be written as

$$Q = \sum_{s_i}^{s_f} \frac{U(s)}{R} \Delta s, \tag{3.8}$$

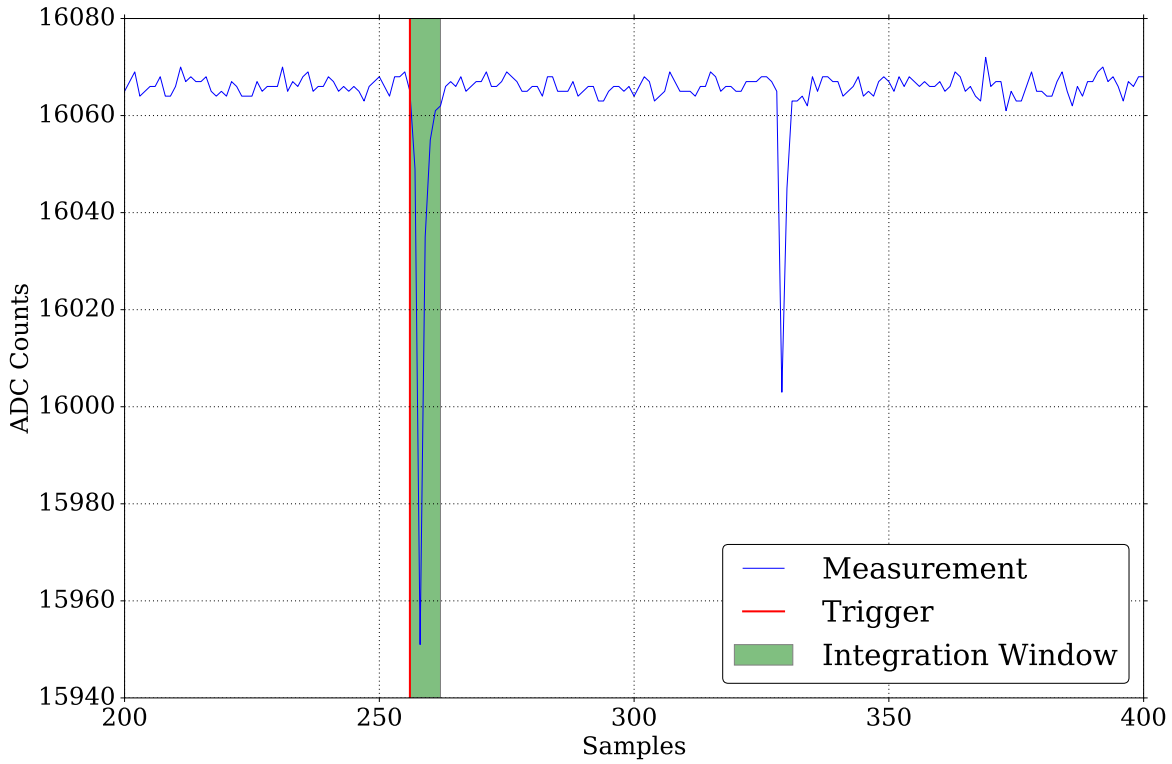

Figure 3.2: ADC counts plotted against the sample number. The smaller peak likely corresponds to a 1 pe event and the larger peak corresponds to a multi pe event. However, this has to be quantified with a large number of events.

where s_i is the first sample and s_f is the last sample of the window. $U(s)$ is the average voltage within the sample s. The gain can now be determined by solving equation 3.3 for μ and exploiting the relation $N_i = Q/e$ and $N_{\mathrm{pe}} = 1$, where e is the elementary charge. One obtains

$$\mu = \frac{Q}{e}. \tag{3.9}$$

Figure 3.3 shows the absolute incidence of the gain values for three different cases in a histogram. If there is no noise in the measuring electronics or in the photomultipliers, the spectrum would consist of multiple δ-functions as shown in the upper panel in figure 3.3. Their amplitudes are determined by the presented poisson statistics. Due to statistical fluctuations of the secondary emission ratio of the dynodes the photoelectron delta peaks are convoluted with a Gaussian function

$$g(x_0, A, \sigma_{\mathrm{dyn}}) = g_{\mathrm{dyn}}(x) = \frac{A}{\sqrt{2\pi}\sigma_{\mathrm{dyn}}} \cdot e^{-\frac{1}{2}\left(\frac{x-x_0}{\sigma_{\mathrm{dyn}}}\right)^2}, \tag{3.10}$$

where A is the area and σ the standard deviation. The convolution of two functions a and b is defined as

$$a * b = \int_{-\infty}^{\infty} a(\tau)b(t-\tau)d\tau. \tag{3.11}$$

According to the properties of the delta function the convolution of a Gaussian function with a delta function returns a Gaussian function. Since the measuring electronics and the PMT electronics are subject to electronic noise, the entire spectrum has to be convoluted with a further Gaussian function $g(x_0, A, \sigma_{\text{elec}})$. The convolution of a Gaussian function with another Gaussian function leads to a Gaussian function again. All in all, the complete spectrum can

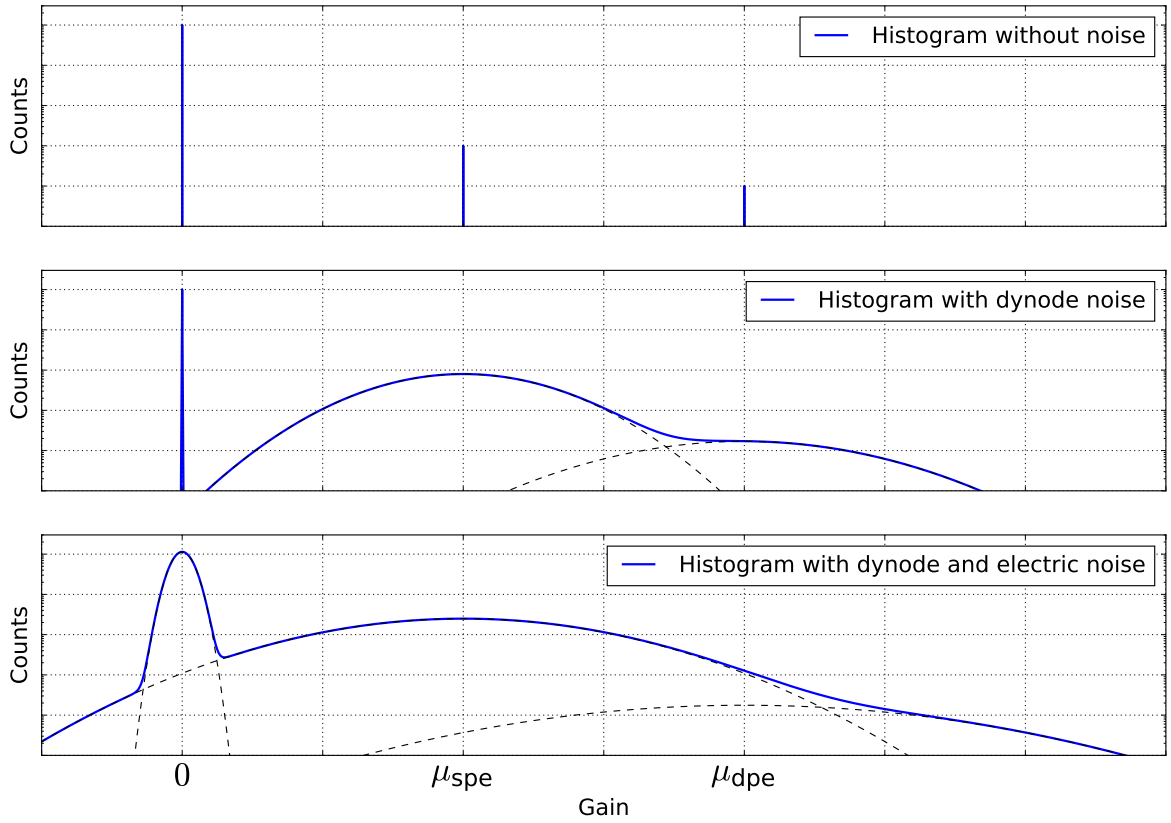

Figure 3.3: Histograms of charge amplification without any noise (top), with dynode noise (middle) and with dynode and electric noise (bottom). The delta function in the middle frame is enlarged, as it is overlaid by the Gaussian function in the lower part of the plot.

be described by a sum of the noise, single-pe (spe), double-pe (dpe) and further multi-pe Gaussian functions [11],

$$f(\mu) = \frac{A_{\text{noise}}}{\sqrt{2\pi}\sigma_{\text{noise}}} e^{-\frac{1}{2}\left(\frac{\mu-\mu_{\text{noise}}}{\sigma_{\text{noise}}}\right)^2} + \frac{A_{\text{spe}}}{\sqrt{2\pi}\sigma_{\text{spe}}} e^{-\frac{1}{2}\left(\frac{\mu-\mu_{\text{spe}}}{\sigma_{\text{spe}}}\right)^2} + \frac{A_{\text{dpe}}}{\sqrt{2\pi}\sqrt{2}\sigma_{\text{spe}}} e^{-\frac{1}{2}\left(\frac{\mu-2\mu_{\text{spe}}}{\sqrt{2}\sigma_{\text{spe}}}\right)^2} + \ldots \tag{3.12}$$

where σ_{noise} corresponds to the electronic noise σ_{elec} and σ_{spe} respectively σ_{dpe} results from the convolution of $g(x_0, A, \sigma_{\text{dyn}})$ with $g(x_0, A, \sigma_{\text{elec}})$.

In oder to investigate the Gaussian nature of the electronic noise it was measured by recording the gain spectrum with the UV-LED switched off. As shown in Figure 3.4, the electronic noise differs for each PMT. The histograms for PMT 11 and PMT 7 are shown in figure 3.4. The electronic noise for PMT 11 differs only slightly from the Gaussian expectation. A very similar noise has been measured for most PMTs. The spectra are shown in the appendix. For PMT channels 6 and 7, the noise differs significantly from the Gaussian shape. This could be caused by the cables and possible interference. The electronics of the used 10x C.A.E.N N979 amplifier can be another source. In the subsequent determination of the PMT gain, the present deviation from the Gaussian shape of the noise must be taken into account.

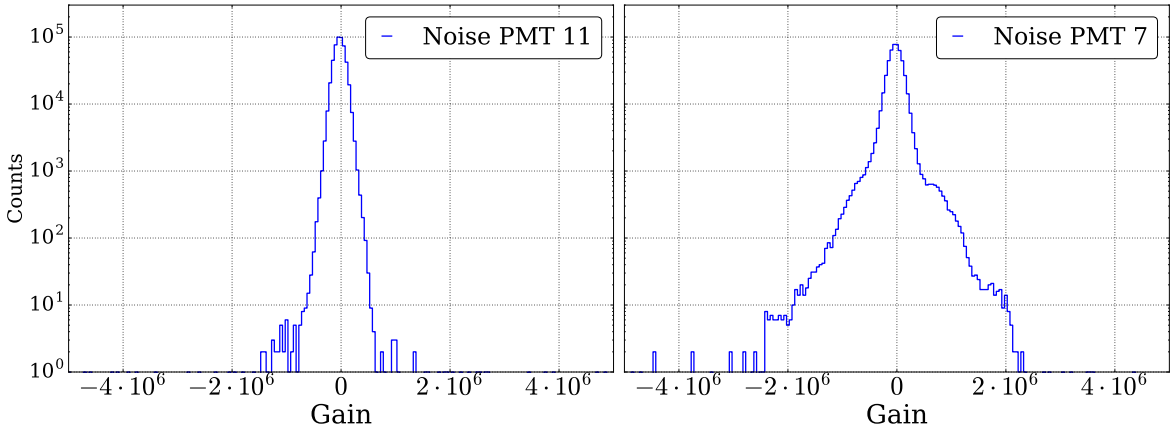

Figure 3.4: Electronic noise of PMT 11 and 7. It was measured with the UV-LED switched off and differs significantly from the Gaussian shape for PMT 7.

3.3 Determination of the PMT gain

In order to account for non Gaussian electronic noise the PMT spectrum is not fitted with the function given in equation (3.12). Instead, a convolution of the histogram without electronic noise as shown in the middle panel of figure 3.3 with the measured electronic noise spectrum is used to determine the PMT gain. The histogram without electronic noise is described by

$$f(\mu) = a_{\text{noise}}\delta(\mu = 0) + g(\mu_{\text{spe}}, A_{\text{spe}}, \sigma_{\text{dyn}}) + g(2\mu_{\text{spe}}, A_{\text{dpe}}, \sqrt{2}\sigma_{\text{dyn}}) + g(3\mu_{\text{spe}}, A_{\text{tpe}}, \sqrt{3}\sigma_{\text{dyn}}) + \ldots, \tag{3.13}$$

where a_{noise} is the amplitude of the δ-function and $g(\mu_{\text{spe}}, A_{\text{spe}}, \sigma_{\text{spe}})$ represents a Gaussian function as introduced in equation 3.10. Since the noise spectra are composed of discrete values a discrete convolution must be used instead of the continuous one given in equation

(3.11). The discrete convolution[1] of two datasets can be performed with the python package numpy.convolve [12] based on the relation

$$(a * b)[n] = \sum_{m=-\infty}^{\infty} a[m]b[n-m]. \tag{3.14}$$

The peaks of the single and multi photoelectron events can be applied directly as a Gaussian function since associativity is valid for convolutions. The summation represented in equation (3.13) is stopped after the fourth Gaussian function, since the areas of the Gaussian functions are determined by the described Poisson distribution and no more measurable influences are expected. The number of free parameters to be fitted is 7. These are the amplitude of the delta function a_{noise}, the four areas of the Gaussian functions A_i, the center position of the Gaussian function μ_{spe} and its width σ_{spe}. The fits were performed as a χ^2 minimization with the python package scipy.optimize.curve_fit [13].

Since the number of photoelectrons emitted by the cathode depends on the quantum efficiency and the number of incident photons, the area of the multi photoelectron peaks is proportional to the UV-LED voltage. In addition the detector geometry must be taken into account since the light of the UV-LED is guided through the top of the TPC. For each PMT, the UV-LED voltage can be varied in such a way that as far as possible no multiple peaks occur, but nevertheless sufficient statistics (at least 10 entries per bin) are obtained in the range of the spe peak. Figure 3.5 shows the fit for PMT 11 with a UV-LED voltage of 5.4 V. The absolute incidence of the charge amplifications is plotted against the corresponding charge amplification. The square root of the incidence was assumed to be the uncertainty of each bin, so that the relative uncertainty of the bins with high event counts converges to zero

$$\lim_{n\to\infty} \frac{\sqrt{n}}{n} = \lim_{n\to\infty} \frac{1}{\sqrt{n}} = 0. \tag{3.15}$$

The fit is shown in red. The individual Gaussian functions of the photoelectron peaks are shown in black. In order to evaluate the goodness of the fit, the reduced χ^2 statistic is calculated for each fit, which is defined as the χ^2 per numbers of degrees of freedom ν:

$$\chi^2_\nu = \frac{\chi^2}{\nu}. \tag{3.16}$$

[1] The discrete convolution could also be performed with the convolution theorem $\mathcal{F}\{a * b\} = \mathcal{F}\{a\} \cdot \mathcal{F}\{b\}$ where $\mathcal{F}(a)$ is the fourier transform of a.

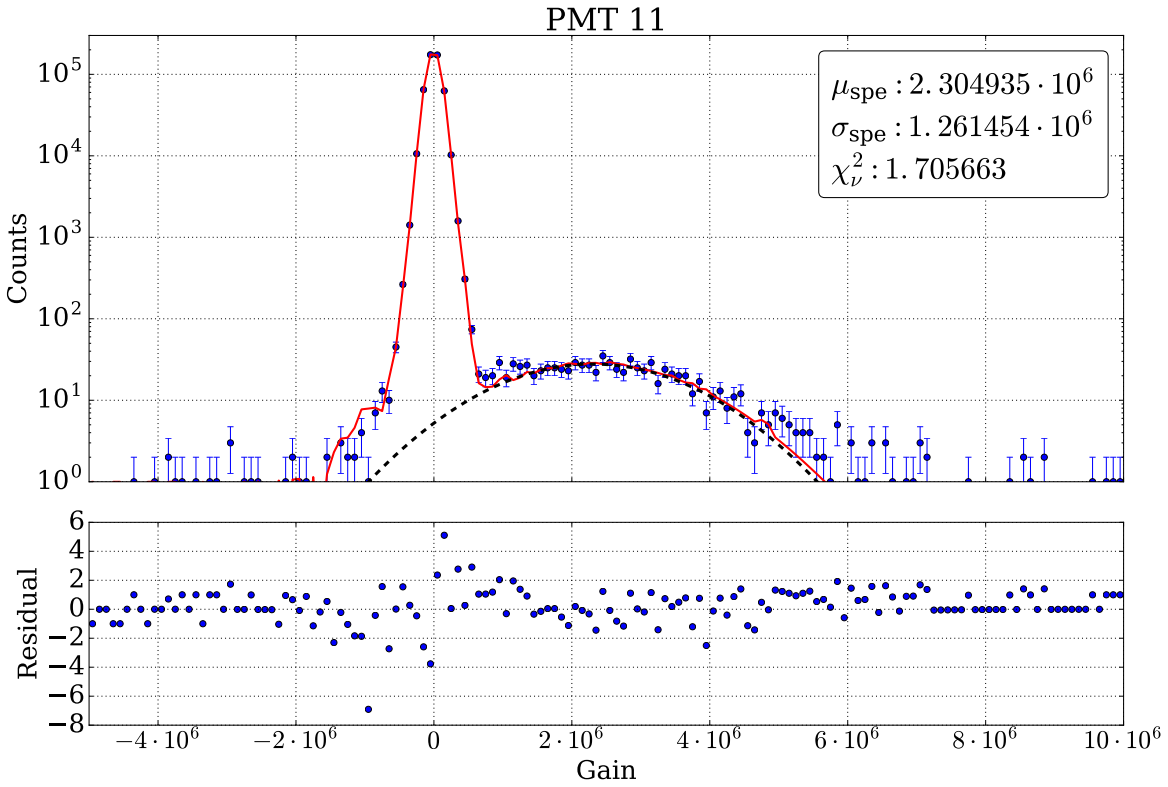

Figure 3.5: Fit of the gain histogram for PMT 11. The measured data is displayed in blue and the fit in red. The Gaussian photoelectron peaks are illustrated as a black dashed line. The fit of PMT 11 is demonstrated, as the residuals show only a comparatively small fluctuation in the area of the pedestal peak.

The number of degrees of freedom corresponds to the number of observations minus the number of fit parameters. χ^2 is defined as the sum of the squared deviations between fit C_i and measured value O_i normalized to the square of the uncertainty σ_i

$$\chi^2 = \sum_i \frac{(O_i - C_i)^2}{\sigma_i^2}. \tag{3.17}$$

A χ^2_ν of 1 corresponds to a good fit since most data points are described by the fit with respect to their uncertainty. Furthermore, the fit quality can be judged by the residuals. These are given together with the fits and defined as the deviation between the fit and the measured value normalized to the uncertainty of each individual data point

$$R_i = \frac{O_i - C_i}{\sigma}. \tag{3.18}$$

The χ^2_ν value is directly proportional to the sum of the squared residuals. The results of the gain determination are given together with the UV-LED voltages of each measurement in

table 3.1. For PMT 5, no value was determined because this PMT was switched off due to a changing baseline.

As shown in table 3.1 some χ^2_ν values are considerably higher than one. Looking at the residuals of the fits shown in figure 3.5 and in the appendix (figures 6.1 to 6.12), it becomes clear that the deviation of the reduced χ^2 is essentially caused by the pedestal peak. Due to its large amplitude the deviations between the fit and the measurement are not visible.

Table 3.1: Results of the PMT gain determination.

Pmt	Gain [10^6]	Gain Sigma [10^6]	χ^2_ν	LED Voltage [V]
0	2.030 ± 0.077	1.268 ± 0.077	1.929692	5.4
1	2.014 ± 0.073	1.209 ± 0.075	10.447612	5.4
2	2.027 ± 0.055	1.338 ± 0.046	2.222912	5.3
3	2.473 ± 0.121	1.779 ± 0.075	12.942493	5.3
4	2.142 ± 0.043	1.194 ± 0.042	9.823719	5.5
5	-	-	-	-
6	2.805 ± 0.268	2.023 ± 0.144	3.276550	5.3
7	2.731 ± 0.160	1.698 ± 0.187	5.748275	5.5
8	2.912 ± 0.133	1.699 ± 0.102	13.986070	5.5
9	2.289 ± 0.053	1.353 ± 0.042	1.565253	5.4
10	2.313 ± 0.046	1.446 ± 0.043	27.138919	5.6
11	2.305 ± 0.075	1.261 ± 0.072	1.705663	5.4
12	2.737 ± 0.062	1.597 ± 0.041	3.293386	5.6
13	2.131 ± 0.040	1.177 ± 0.034	1.881886	5.4

The noise peak affects the χ^2 fit more than the peaks of interest due to small relative errors compared to the spe and multi pe peaks. In order to weight them more prominently in the fit all uncertainties are changed manually so that bins with many entries have a larger relative error compared to bins with lower statistics:

$$\Delta N = \sqrt{\sqrt{N}^2 + (r \cdot N)^2}. \tag{3.19}$$

As the uncertainties of each data point are increased the χ^2_ν is reduced. In order to estimate the influence of the modified uncertainties on the calculated gain, the parameter r is varied between 0 and 0.1. Figure 3.6 shows the fitted gain as a function of r for PMT 1. The plotted uncertainties result from the fit. It can be seen that for PMT 1 the gain increases slightly with increasing r. The values are consistent within the context of the uncertainty of the originally determined gain. However, a clear tendency is not evident for every PMT. For PMT 4 there is a reduction of the gain and then an increase. This is shown in figure 3.7. The Plots for all other PMTs can be found in the appendix. For each PMT, the maximum

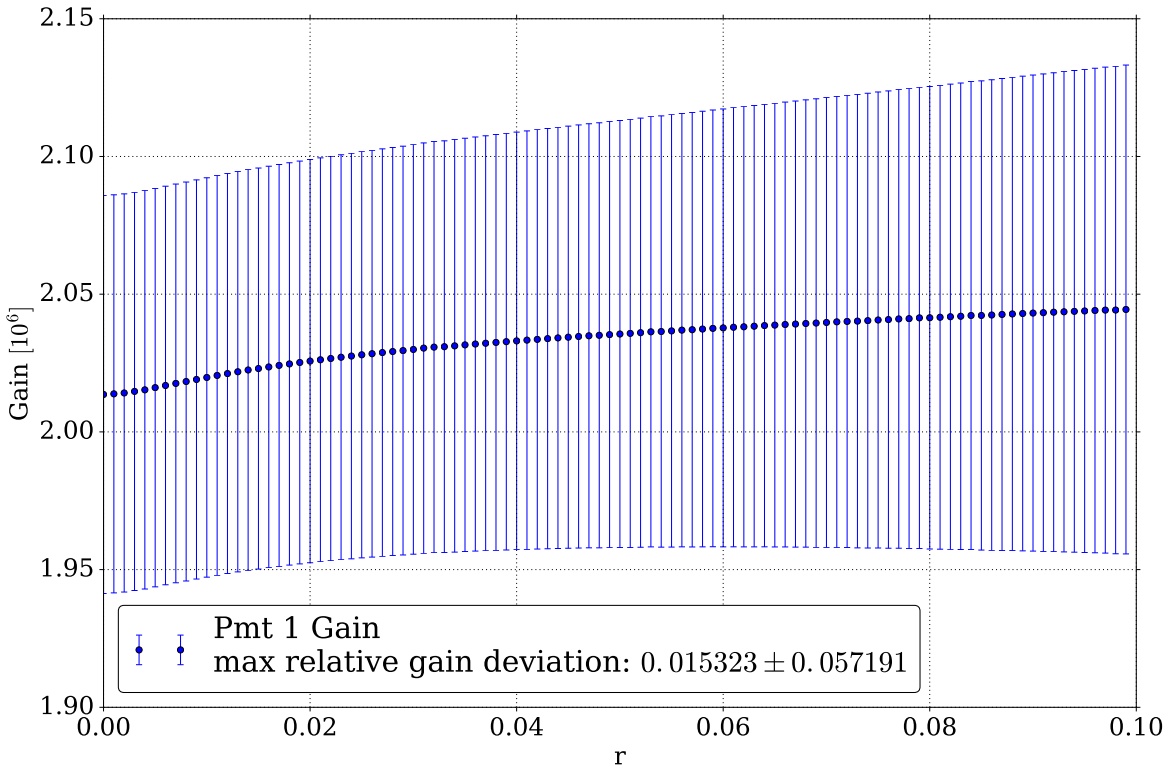

Figure 3.6: Result of the gain determination of PMT 1 plotted against r. The drawn uncertainties result from the fit. The total change in the gain is within the range of the uncertainty of the initial value.

relative deviation $\mu_{(\text{rel dev})}$ from the gain μ for $r = 0$ specified in table 3.1 is calculated with $0 < r < 0.1$

$$\mu_{(\text{rel. dev})} = \frac{|\mu_{\max} - \mu|}{\mu}. \tag{3.20}$$

Here, $\mu_{\max}$ is the gain value with the highest deviation from μ. The uncertainties of this deviation were determined with equation 6.1 given in the appendix. The resulting values are listed in table 3.2. It is evident that only PMT 7 has a maximum relative deviation that

Table 3.2: Maximum relative gain deviation for each PMT

Pmt	$\mu_{\text{rel. dev}}$	Pmt	$\mu_{\text{rel. dev}}$	Pmt	$\mu_{\text{rel. dev}}$
0	0.006 ± 0.060	5	-	10	0.025 ± 0.030
1	0.015 ± 0.058	6	0.045 ± 0.161	11	0.005 ± 0.048
2	0.016 ± 0.042	7	0.072 ± 0.095	12	0.030 ± 0.035
3	0.024 ± 0.076	8	0.046 ± 0.072	13	0.025 ± 0.030
4	0.038 ± 0.023	9	0.011 ± 0.035	-	-

exceeds 5 %. Furthermore, the specified uncertainties for all PMTs, with the exception of PMT 6 and 7, are larger than the maximum relative gain deviations. Figure 3.8 shows the fit for PMT 1 achieved with $r = 0.1$.

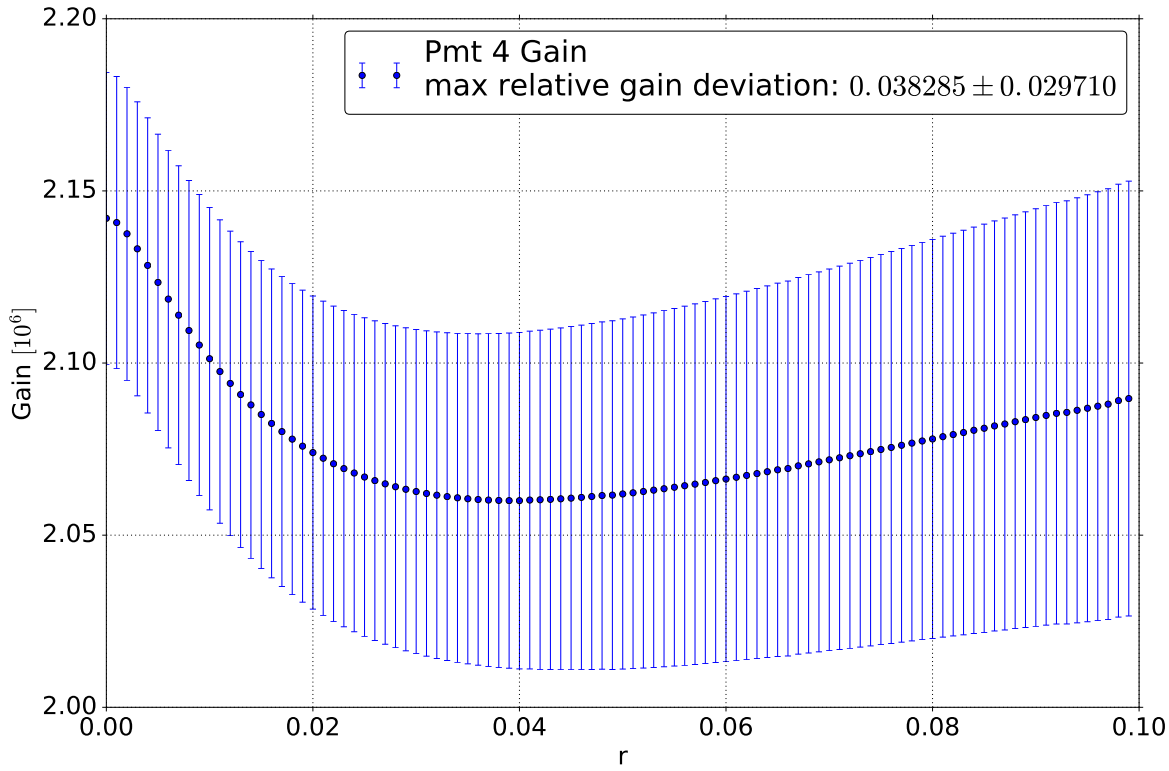

Figure 3.7: Result of the gain determination of PMT 4 plotted against r. The uncertainties result from the fit. The total change in the gain is still within the range of the uncertainty of the initial value.

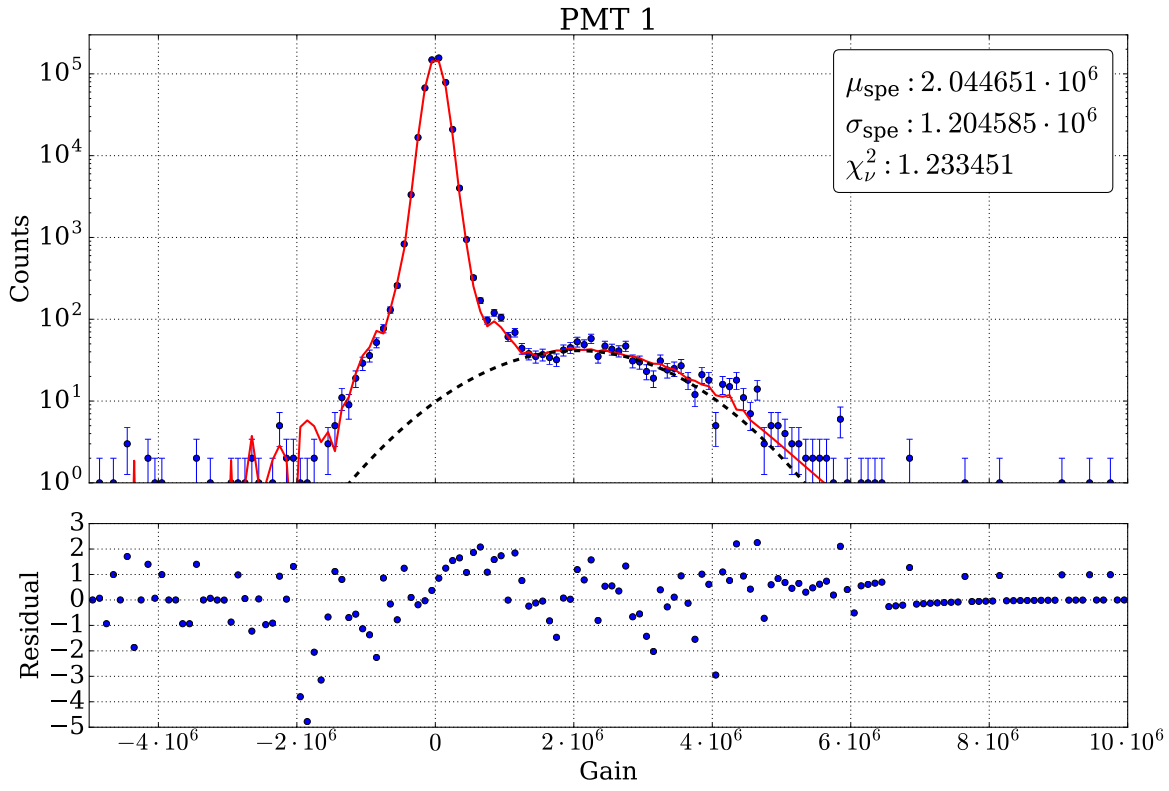

Figure 3.8: Fit of the gain histogram for PMT 1 with modified uncertainties for $r = 0.1$.

The residuals now fluctuate around 0 and do not show a distinct peak structure anymore. Since the values specified in table 3.1 change only insignificantly as a result of the modification of the errors, and the uncertainty of the maximum relative deviation is greater than the actual change, the values determined for $r = 0$ are regarded as plausible. Thus, they can be used for data processing.

The previously determined gain values are used to deduce the number of photoelectrons emitted at the cathode from the voltage drop at the PMT anode. For this purpose, the voltage drop caused by a single emitted photoelectron must be determined first.

$$\begin{aligned} \mu \cdot e = \quad & Q & &= \frac{U}{R} \cdot t \\ \Rightarrow U = \quad & \tfrac{\mu \cdot e \cdot R}{t} & &= 1.602\,\mathrm{mV} \end{aligned} \tag{3.21}$$

Equation 3.9 and the relation $Q = \frac{U}{R} \cdot t$ were used. Furthermore, $R = 50\,\Omega$ and $t = 10\,\mathrm{ns}$ have been used for the calculation. A value of $\mu = 2 \cdot 10^6$ was assumed as gain. Since a 10x amplifier is used, a voltage drop of 16.02 mV is transmitted to the Analog Digital Converter which has an input range of 2.25 V distributed over 2^{14} channels. This means that one photoelectron corresponds to about 117 ADC counts. Using this conversion, the number of photoelectrons of any signal can be determined from the ADC counts.

4 Liquid level calibration

Since the appearance of S2 signals depends on the extraction of the electrons from the liquid and this, in turn, depends on the liquid level, it is important to adjust the level optimally. As the electrons are extracted by the extraction field between the gate and the anode, the optimal level is expected above the gate but below the anode. To check this the determination of the liquid level in the Münster TPC is described first. Afterwards, the measurements are explained and evaluated for the optimization of the liquid level.

4.1 Determination of the liquid level

The filling height within the Münster dual phase time projection chamber can be determined with three capacitance-based level meters [14]. Such a level meter consists of a steel rod surrounded by a steel tube. Both elements are isolated from each other by a polyether-ether-keton spacer. The level meters are mounted in the TPC in such a way that a liquid and a gaseous xenon phase are present in the inner part. Due to the different dielectric constants of liquid and gaseous xenon the capacity of the level meter changes with the liquid level. It can be measured with an LCR-Meter and has to be calibrated before the filling height can be determined.

Since not all three level meters can be read out at the same time, only one level meter is evaluated for the following determination of the liquid level. This enables a more precise temporal resolution during the calibration of the level meter as the LCR meter does not have to read each level meter alternately. The level meter can be calibrated during the filling of the TPC as long as the flow of the incoming xenon is constant and known. Figure 4.1 shows the flow of the xenon during filling. It is constant over the entire time period under consideration. In the plot the value specified for the flow is the mean value of the measured data. The standard deviation is used as the uncertainty which results from the inaccuracy of the flow controller. The increase of the liquid level within the TPC is divided into two sections. This is owned to the construction of the TPC which is shown in figure 4.2.

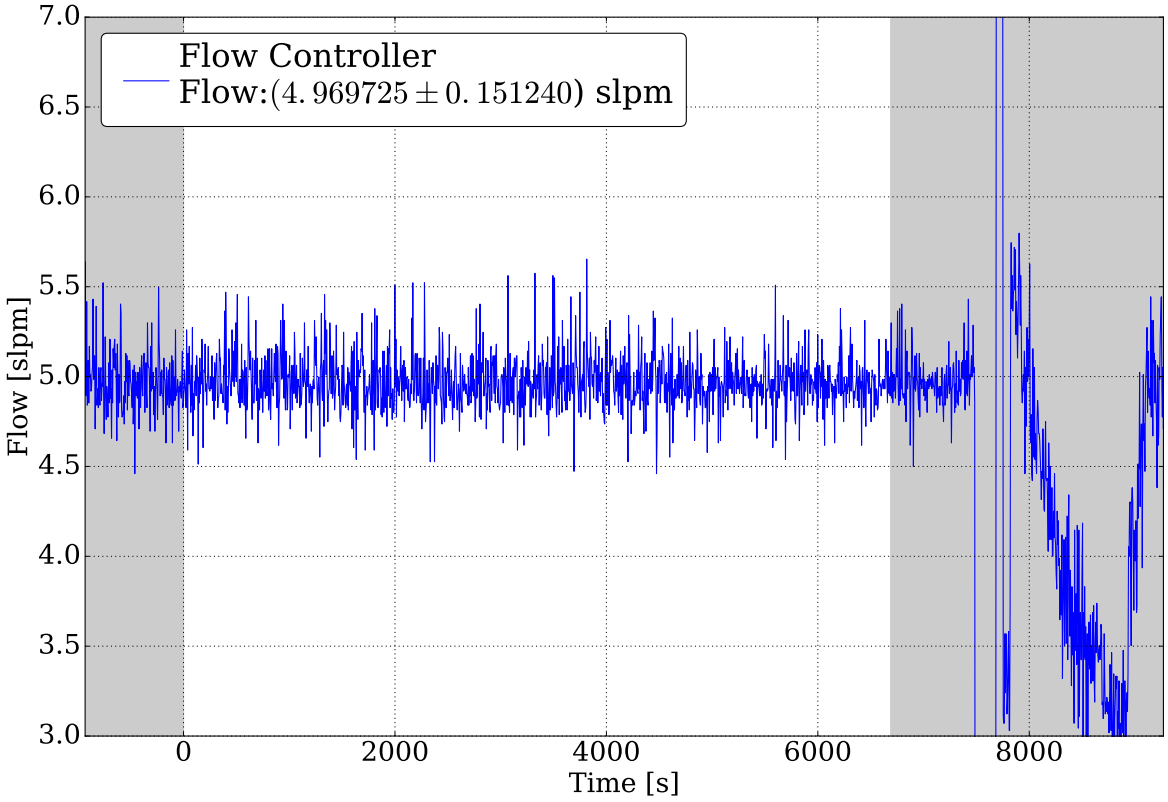

Figure 4.1: Flow of the incoming xenon during TPC filling plotted against the time. The time zero point was set to the time of immersion of the bottom PMTs. The periods not considered are marked in gray.

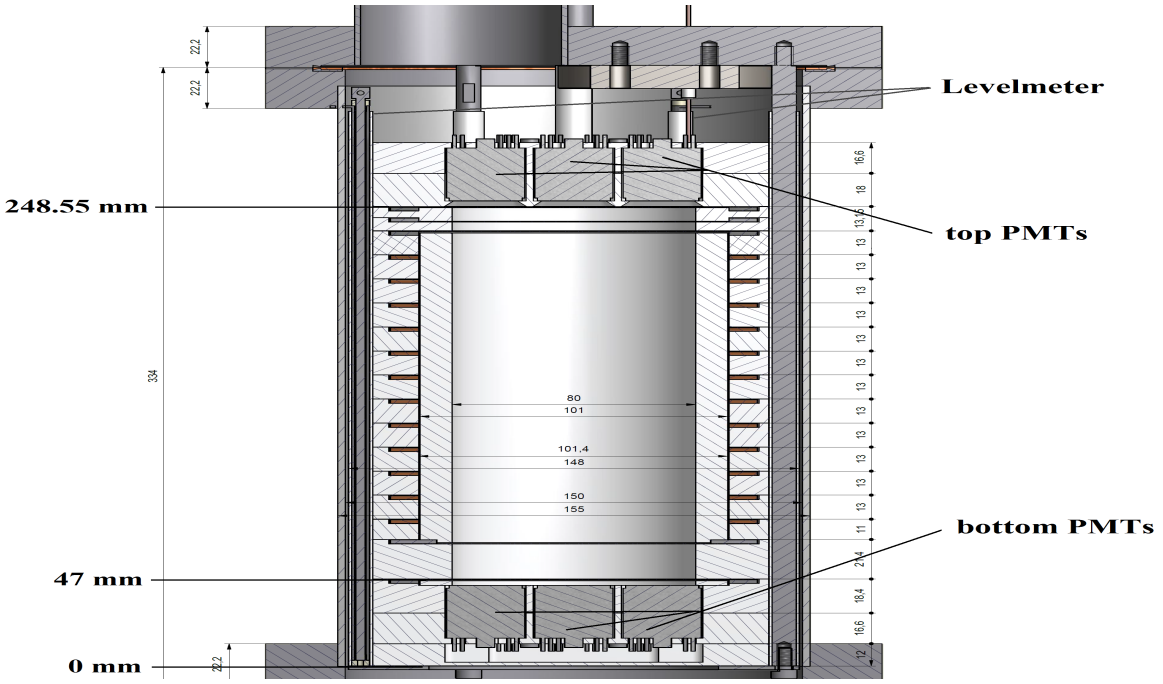

Figure 4.2: Technical drawing of the TPC [14]. In the lower area the PMTs are visible, which are responsible for the faster rise of the liquid level in this section.

As the base area of the volume accessible for xenon is constant within the sections, the level increase is linear. However, the gradient of the increase changes at a certain point. Seven PMTs are mounted in the lower part of the cylindrical volume which reduce the volume available for the xenon. This results in a faster liquid level increase compared to the section above the bottom PMTs. As soon as the PMTs are completely immersed in the liquid xenon the liquid level rises more slowly. At this point a filling height of 47 mm is reached, which can be used as a fixed point for the determination of the liquid level above the PMTs. This point was set as the time zero of the figures 4.1, 4.3 and 4.4. Once the gate temperature sensor is reached the filling is stopped. This sensor is located at a height of 240.1 mm and can be used as a second fixed point. Since the liquid level above the bottom PMTs is of interest, the lower fixed point is assumed to be the zero point, the upper fixed point than has a height of 193.1 mm. Figure 4.3 shows the temperature of the gate temperature sensor plotted against the time. The temperature of the gate sensor drops sharply as soon as it dips into the liquid xenon. The periods highlighted in gray are not used for calibration as they are outside the fixed points and the assumptions made are no longer valid in these areas of the TPC. Considering the increase in the level meter capacity in the relevant temporal range

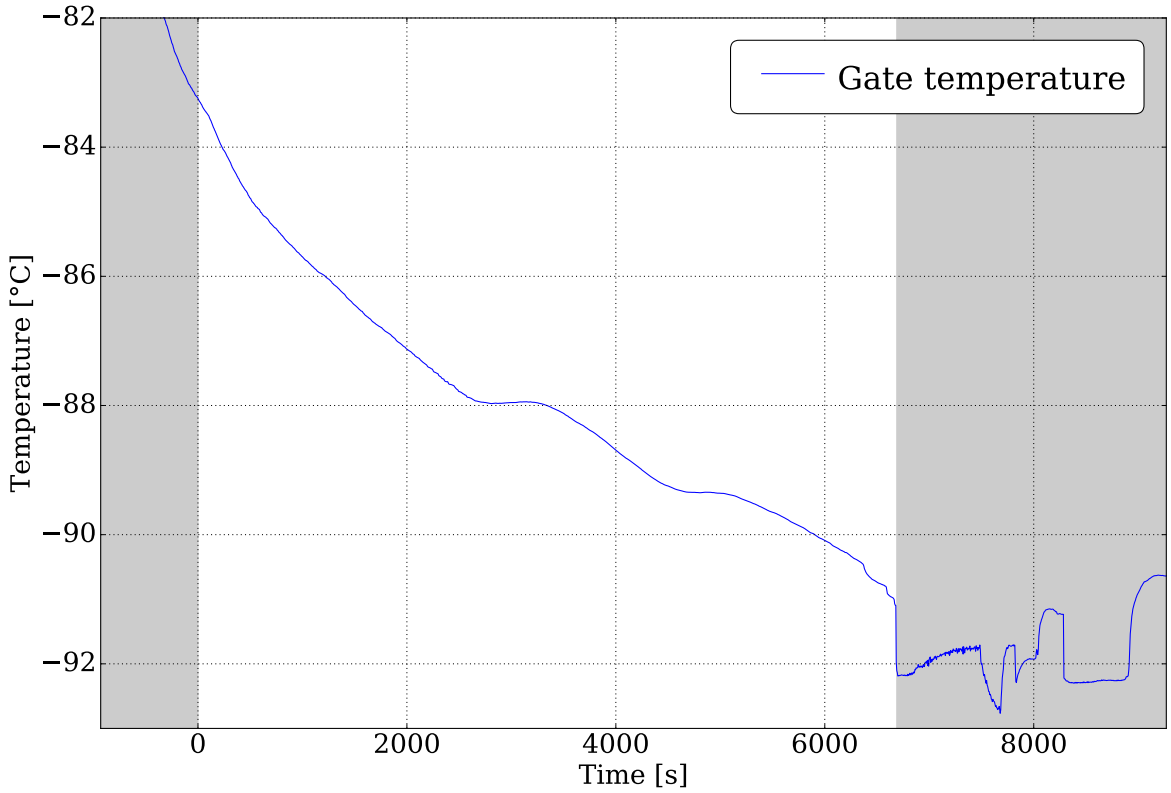

Figure 4.3: Temperature of the gate temperature sensor plotted against the time. The time of the sharp temperature drop is used to determine the second fixed point for the level meter calibration. The temperature fluctuates after completion of the filling process, as the gas circulation has been started in the system.

a linear increase in capacity can be observed. This is represented in figure 4.4 and illustrated by a linear fit with the function

$$y = a \cdot t + b. \tag{4.1}$$

Here, a is the slope, b the offset, y the capacity and t the time. In the left gray marked area of the graph the linear increase of the capacity with higher slope can be observed as described with the bottom PMTs. The linear fit accurately describes the increase in capacity in the area under consideration. However, there is a slight oscillation in the residuals, which can be attributed to possible pressure and temperature changes in the gas system that affect liquefaction of the xenon. Since both the filling height and the capacity of the level meter

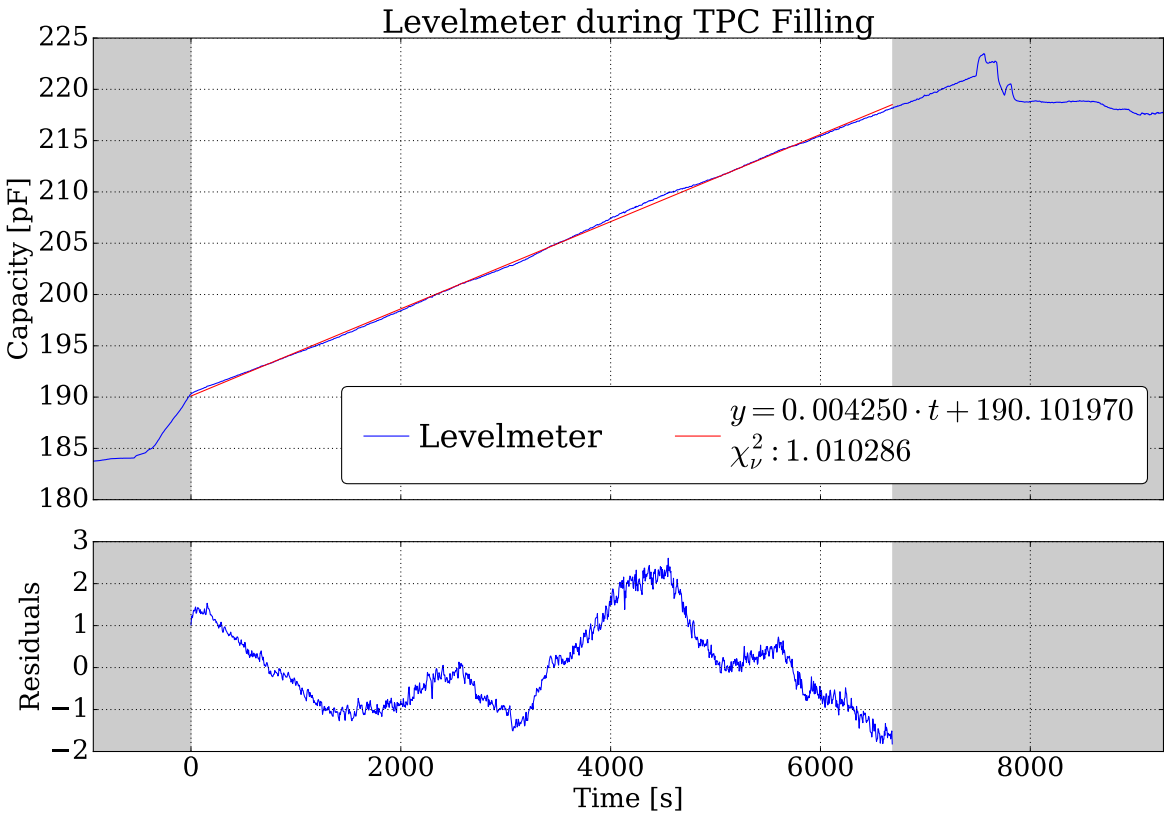

Figure 4.4: Level meter capacity during TPC filling plotted against the time with linear fit.

increase linearly in time the level meter capacity can be converted into a height by a linear transformation. As the time of reaching the fixed points cannot be determined without uncertainty, the capacity is averaged in a time interval of ±30 s around the fixed points and the standard deviation of the values is used as the uncertainty. This leads to errors in both the specified slope and offset.

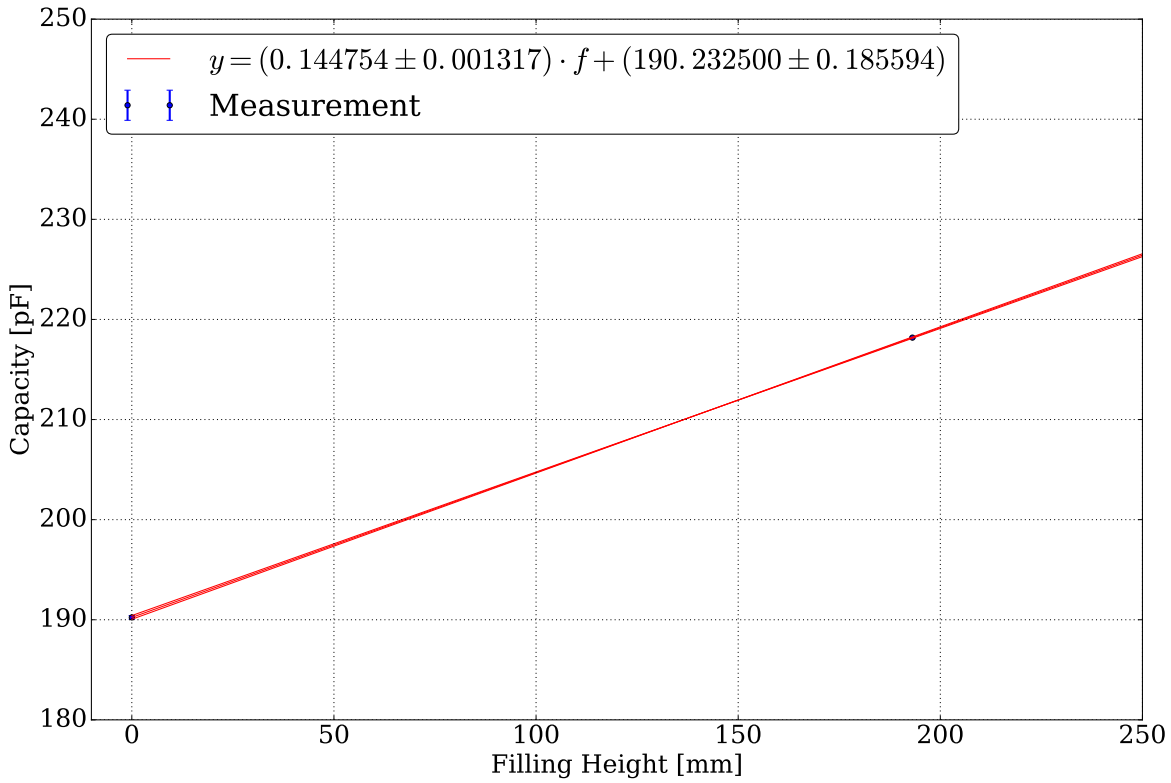

Figure 4.5: Capacity of the level meter plotted against the filling height. The two fixed points are marked in blue and the linear interpolation in red. The shaded area indicates the uncertainty of the linear model.

Two further lines are calculated manually which take into account the maximum (minimum) offset and the minimum (maximum) slope. The mean deviation from the initial line is then used as uncertainty. As shown in figure 4.5, the slope and offset can be determined with a relative accuracy of less than one percent. To infer the fill level from the capacitance equation (4.1) must be solved for the level

$$\begin{aligned} f(y) &= \frac{1}{a} \cdot y - \frac{b}{a} \\ &= (6.6531 \pm 0.0383)\,\frac{\text{mm}}{\text{pF}} \cdot y - (0.005487 \pm 0.000004)\,\text{mm}. \end{aligned} \tag{4.2}$$

The uncertainty of the conversion is determined by an error propagation according to equation (6.2) given in the appendix. The uncertainties of the slope a and the offset b result from the linear fit and the uncertainty of the measured values y. If one compares the slope of the line shown in figure 4.5 with the value of $0.161\frac{\text{pF}}{\text{mm}}$ determined in [14], it can be stated that the value determined in this calibration is lower. This can be caused by the different choice of the second fixed point.

4.2 Measurements with the filled TPC

As already mentioned, a physical event in a TPC should produce one S1 signal followed by an S2 signal. Since the appearance of S1 signals does not depend on the liquid level, the optimum level must be determined by the occurrence and quality of the S2 signals. The optimum fill level is characterized by the highest possible rate of physically meaningful S2 signals.

4.2.1 Trigger and raw data processing

In order to ensure that only events containing an S2 signal are stored during data acquisition different properties of the S2 signal can be used. As already mentioned, S2 signals generate a much higher light intensity than the corresponding S1 signals. Furthermore, a typical S2 lasts longer than an S1. These properties of the S2 can be used to define a trigger threshold for each of the 14 PMTs. As soon as a signal with more than 150 ADC Counts i.e. 1.3 photoelectrons above the baseline is registered on one of the PMTs, which exceeds this threshold for 30 samples i. e. 300 ns, the data of all PMTs are stored as an event. Each event contains in total 16000 samples whereby 2000 samples are stored after the trigger. This ensures that even events which are located deep in the TPC and, therefore, have a longer time between the S1 and S2 signal are recorded.

The raw data are processed with the *Processor for Analyzing Xenon* (PAX) [1]. Using the PMT gains PAX converts PMT signals into physically meaningful data that can be analysed. This includes position reconstruction, the classification of S1 and S2 signals as well as the rejection of noisy signals. PAX was developed for the direct dark matter search experiment XENON1T and adapted for use with the Münster TPC. Further information on the setup of the data acquisition system and data processing can be found in [15].

4.2.2 Measurements

In order to determine the optimum liquid level of the xenon in the TPC ten measurements were taken at different levels while ^{83m}Kr as a radioactive source was continuously injected into the detector system. The liquid level can be modified by two processes. If the flow of the xenon in the gas system is reduced the liquid level increases. Since the flow cannot be chosen arbitrarily small, additional xenon must be filled to the TPC as a second method. In figure 4.6 the records of the level meter for the whole measurement campaign are plotted against time. All measurements were taken over a period of six days and are marked in color in figure 4.6. For each measurement the capacity of the level meter is averaged and

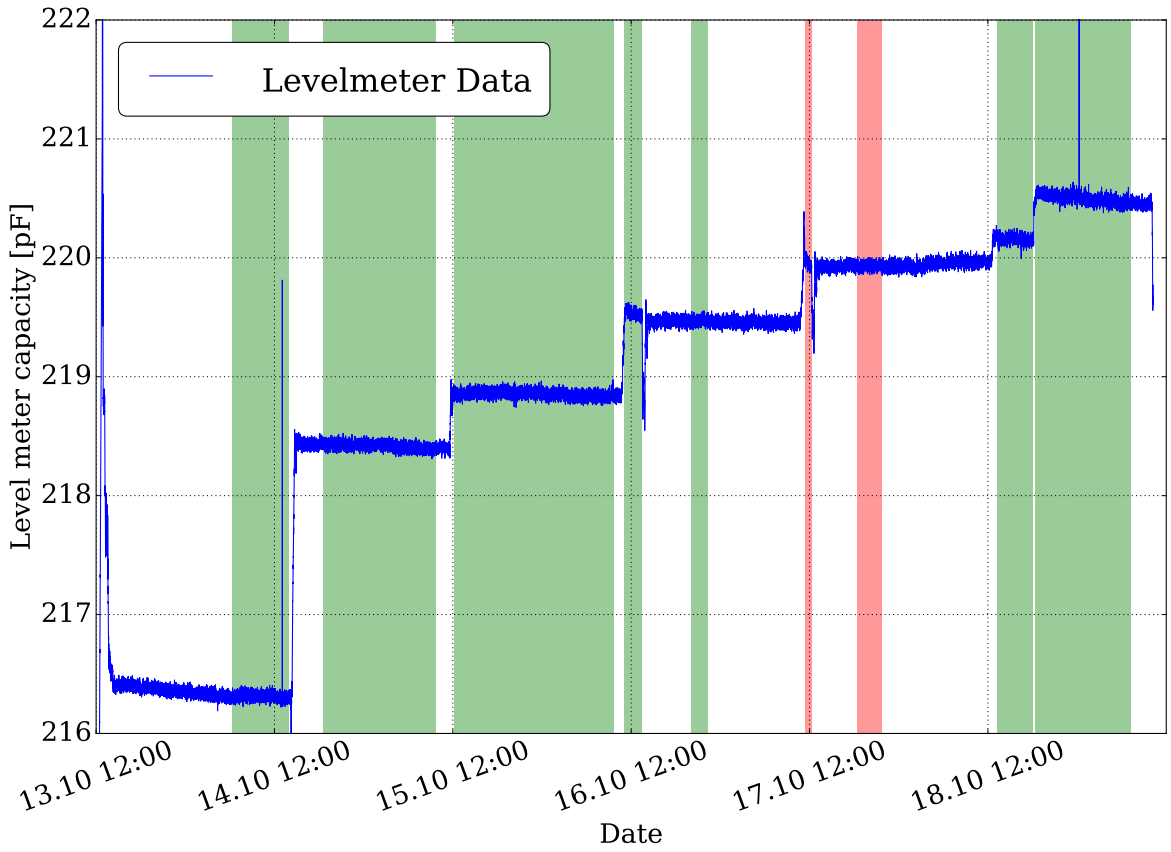

Figure 4.6: Level meter capacity plotted against time. The time periods in which a measurement was performed are highlighted in color. The red marked measurements were taken with the best liquid level. On 16th and 17th october a temporary decrease of the liquid level can be observed. The previous increase was achieved by changing the flow. The short-term decline resulted from the increase in flow and the subsequent increase was caused by the addition of xenon. Due to the short measuring time of measurement 4 it is difficult to distinguish from measurement 5. Both measurements were performed on the 16th october.

converted into a filling height with equation (4.2). The standard deviation is considered as the uncertainty of the capacity data and the possible uncertainties of the levels are determined with equation (6.2). The durations and the calculated filling heights of the measurements are given in table 4.1. It should be noted, that the uncertainties indicated for the liquid level are not independent of each other, as they are caused by the uncertainties of the level meter calibration. The uncertainty of the calculated filling height includes the uncertainty from equation 4.2 and the uncertainty of the level meter capacity. As a result, all filling heights deviate either downwards or upwards in the context of uncertainties.

Table 4.1: Measuring time and liquid level of the performed measurements. The measuring time varies as sufficient statistics are required for each measurement.

Measurement	Measuring time [s]	Liquid level [mm]
1	27314	180.2 ± 2.2
2	54392	194.7 ± 2.2
3	77494	197.7 ± 2.3
4	725	202.3 ± 2.3
5	7275	202.4 ± 2.3
6	7886	202.0 ± 2.3
7	3098	205.3 ± 2.3
8	11801	205.2 ± 2.3
9	17245	206.7 ± 2.3
10	46396	209.1 ± 2.4

4.2.3 Rate vs. level

Now that the filling height of each measurement is known, the rate of S2 signals is examined in relation to the filling level. Since a recorded event can also contain several S1 and S2 signals, the largest S1 and S2 signals are most likely caused by the ^{83m}Kr decay due to the high activity of the source. In order to determine the rate of these S2 signals a histogram of the recorded times is created and the entry of each bin is normalized to the width of the bin. This gives the number of S2 signals per second which is equivalent to the S2 rate and can be monitored over time as shown for measurement 8 in figure 4.7. The observed

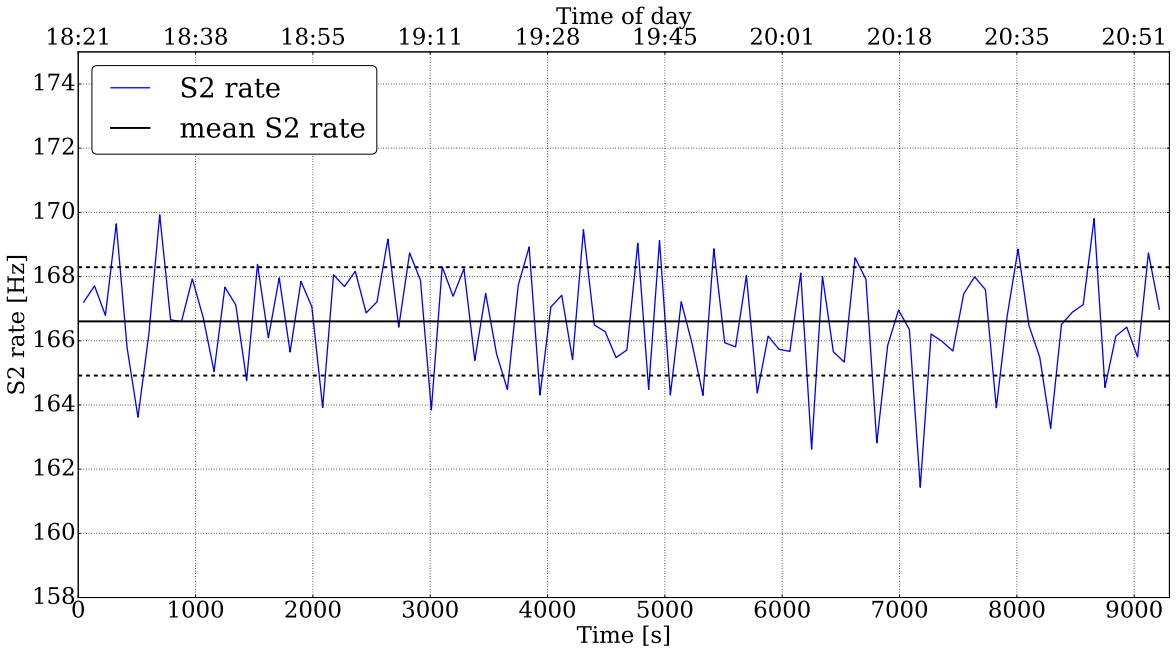

Figure 4.7: Rate of S2 events plotted against the time. The mean S2 rate is marked in black and the uncertainty as dashed lines.

rate for this measurement is constant over time, but varies in the order of a few Hertz. For each measurement the mean S2 rate is determined and the standard deviation is used as the uncertainty. By comparing the rates for each level a strong increase in the S2 rate can be seen from 202 mm upwards. This is shown in figure 4.8. The highest rate has been achieved for measurement 8. For higher filling levels the event rate decreases to approximately 1 Hz. This is caused by the anode being immersed in the liquid xenon. At this point no electrons can be extracted from the liquid anymore, which leads to a lack of S2 signals. The range

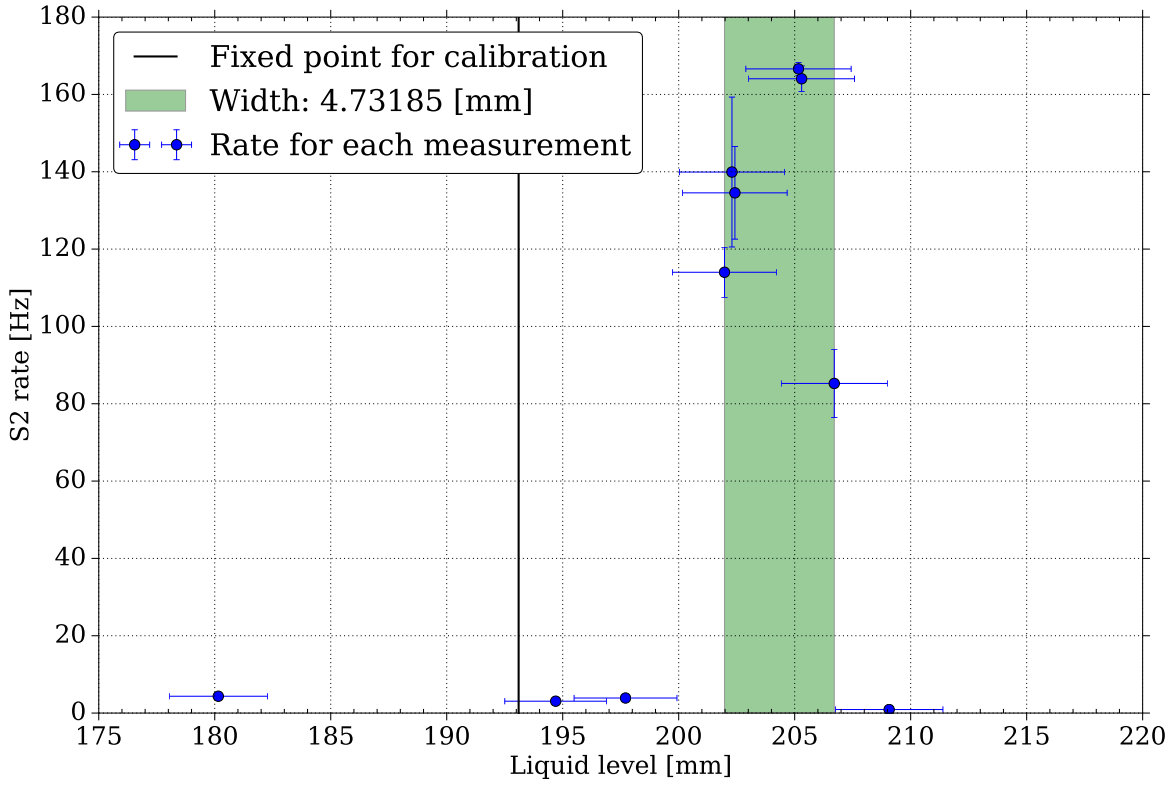

Figure 4.8: Mean S2 rate of each measurement plotted against the liquid level in the TPC. The second fixed point is marked in black.

of the zone with high S2 rate is $d = 4.73\,\text{mm}$ and was determined from the level difference between measurements 6 and 9. The uncertainties of the points are not taken into account here, as they are not independent of each other and all measured values deviate uniformly downwards or upwards within the given uncertainty. The gate and the anode of the Münster TPC are 5 mm apart from each other, which is in agreement with the determined width of the gas gap producing S2s of 4.73 mm.

The position of the temperature sensor at the gate is additionally displayed in figure 4.8 in order to compare this with observed event rates. A high event rate is to be expected as soon as the gate dips into the liquid xenon. The calculated liquid levels of the measurements with the high S2 rates do not match this expectation. This can be caused by different sources

of error during level meter calibration. If, for example, the temperature sensor at the gate is cooled down before the liquid level has reached the bore of the sensor, the fixed point is assumed to be lower than it actually is. Such an early cooling can be caused by drops of liquid xenon splashing out of the possibly boiling liquid phase. In addition, capillary effects within the level meter could lead to an inaccurate determination of the level.

4.2.4 Ratio of S2 Area vs. S1 Area for different levels

Another parameter of interest is the ratio of S2 area and S1 area called S2/S1 in the following. The area of the signals is stated in photoelectrons and is a metric for the deposited energy of an interaction inside the TPC. The parameter S2/S1 describes the strength of the S2 signal in relation to the corresponding S1 signal. As the S2 signal strength depends on the width of the gas gap S2/S1 should exhibit variation with the liquid level. For each event the ratio is calculated and filled into a histogram which is presented in figure 4.9 for measurement 8. The plots of the other 9 measurements are given in the appendix.

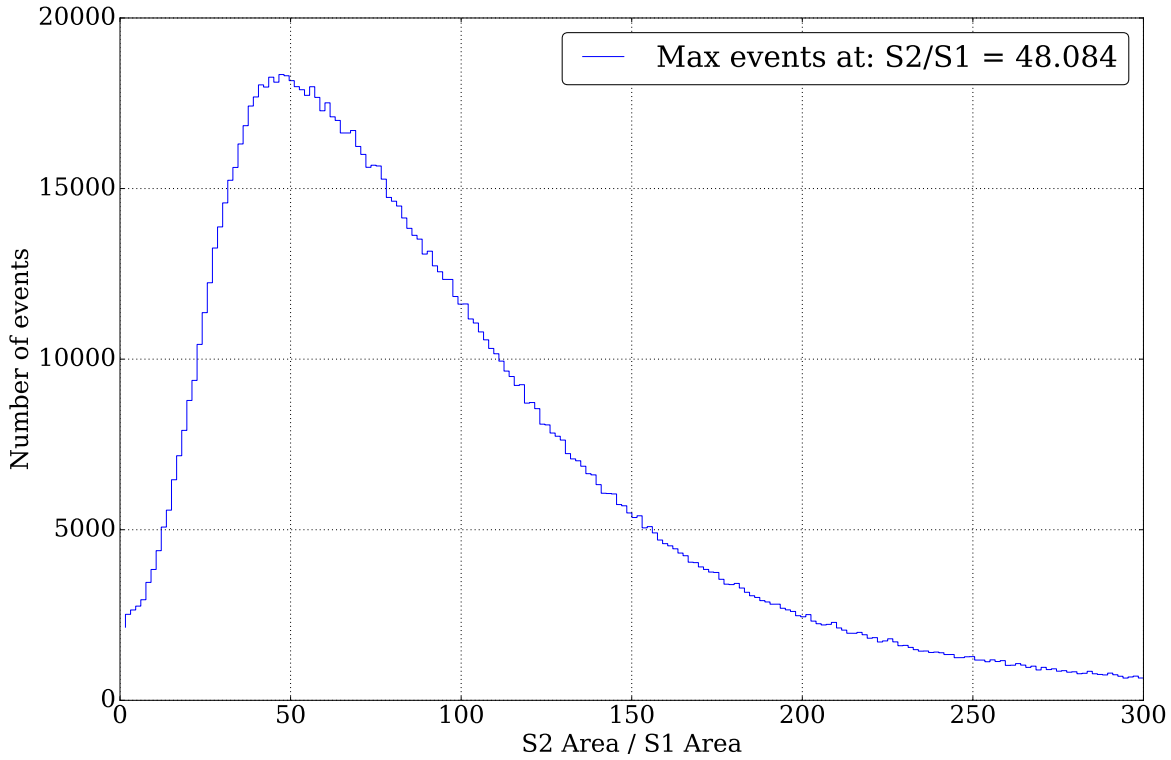

Figure 4.9: Histogram of the S2 area S1 area ratio for measurement 8. The S2/S1 ratio is an indicator for the occurrence of physically meaningful S2 signals.

As seen in the histogram, there is a most frequent S2/S1 ratio. The number of events increases with increasing S2/S1 and reaches its maximum at approximately S2/S1 = 48.1.

Subsequently, the counts decrease. By plotting the most frequent ratio of the S2/S1 against the liquid level figure 4.10 is obtained.

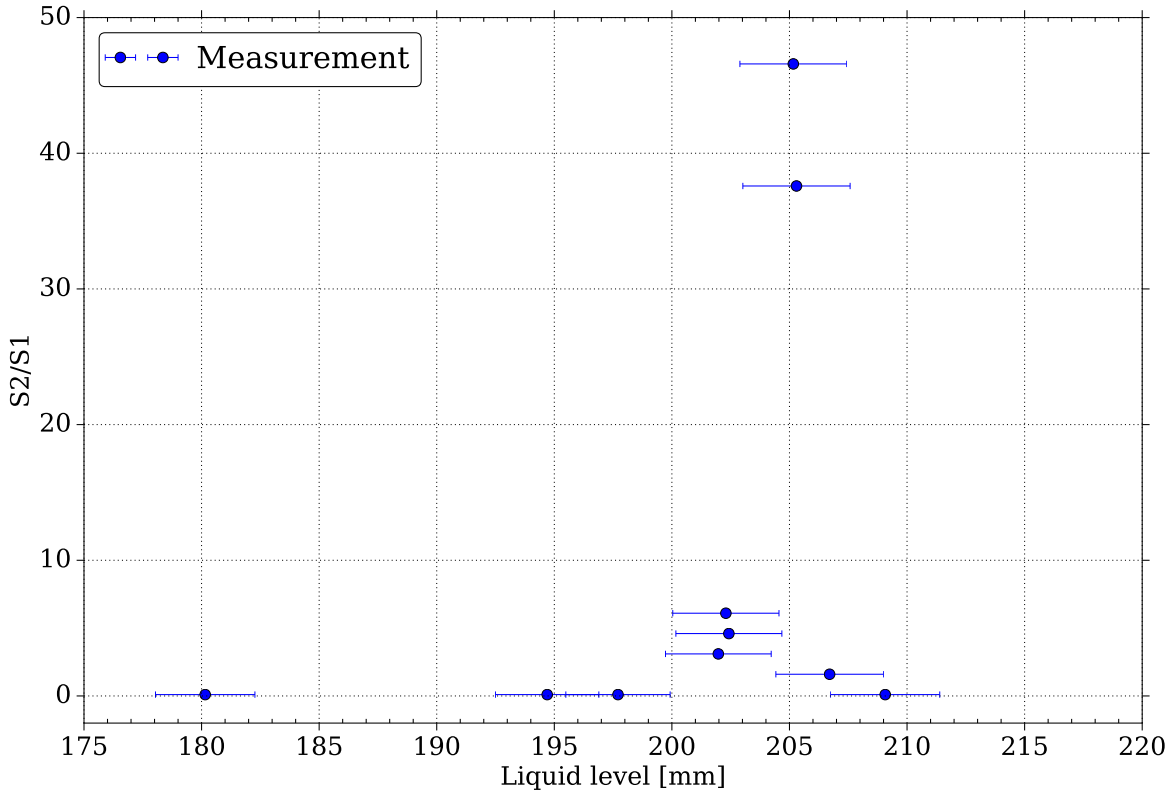

Figure 4.10: Most frequent S2/S1 plotted against the liquid level. Compared to figure 4.8 the increase of S2/S1 is much more sensitive to the liquid level.

A rise of S2/S1 from a liquid level of approximately 202 mm is visible. However, the S2/S1 ratio is much more sensitive to small liquid level changes than the event rate. The maximum S2/S1 is reached at a liquid level of 205.2 ± 0.23 mm. The highest S2 rate was also measured at this level. Since the strength of the S1 signal does not depend on the liquid level one can obtain that the strength of the S2 signal is strongly dependent on the level. If the liquid gas interface is located between the gate and the anode, it can be assumed that the number of electrons reaching the interface is constant. Thus, the strength of the mean S2 signal depends on the number of extracted electrons and the distance between the interface and the anode.

It is desirable for data acquisition and subsequent analysis to measure the strongest possible signal. The filling level must be selected in such a way that the S2/S1 area ratio is maximized at a constant electric field. Since the absolute liquid level can only be determined inaccurately by a single level meter, various measurements with ^{83m}Kr must be taken for the next filling of the TPC to ensure that the optimum level is reached.

A technical solution is to use all three built-in level meters. For this purpose, it would be necessary to read the data of all three level meter simultaneously. Furthermore, a shorter level meter in the area of the gate and the anode could be used to determine and adjust the liquid level more precisely. However, such structural changes of the TPC are time-consuming.

An easier method to implement is to adjust the liquid level according to the S2 rate and S2/S1 ratio. The liquid level should be increased until a significant increase in the event rate is observed. This is a good indicator that the liquid gas interface is located between the gate and the anode. As this does not automatically correspond to a high S2/S2 ratio as seen before, this value must then be determined and maximized by slightly changing the liquid level with ^{83m}Kr in the detector.

4.2.5 First look into ^{83m}Kr data

Once the optimum liquid level has been found, it can be investigated whether the signals generated by ^{83m}Kr decay can be identified in the recorded data of measurement 8. Figure 4.11 shows a two-dimensional histogram of the S1 and S2 area. The uncut data shows the highest population for a S2 area of less than 5000 pe and an S1 area of less than 100 pe. To verify whether the observed population is of physical origin, two cuts are performed. Cuts exclude certain events based on previously defined conditions. In this case events that likely do not originate from the decay of ^{83m}Kr are discarded.

The first condition is that only events that have occurred in the middle part of the TPC are considered further on. All events that are closer than 2 cm to the gate or cathode are excluded.

Since the radioactive source used was ^{83m}Kr which decays to ^{83}Kr via an intermediate step with a half-life of 154 ns, all events are cut where the time difference between the largest S1 and the second largest S1 is more than 600 ns. This is based on the assumption, that the 32.1 keV and 9.4 keV decays generate the largest and second largest S1s. Due to the short half-life 93.3% of the secondary decays will occur within the first 600 ns after the 32.1 keV decay.

The resulting S1-S2 histogram is shown in the right part of Figure 4.11. It can be seen, that the previously described population remains largely unchanged, whereas the frequency of the other bins is significantly reduced. If the number of events remaining after the cuts is now plotted against the depth in the TPC and the area of the S2 signal, a decrease of the S2 area with increasing depth in the TPC is visible as shown in figure 4.12. Assuming that the observed population is generated by the same source, the loss of drifted electrons due to the attachment to electronegative impurities can be observed in this plot. As the probability of

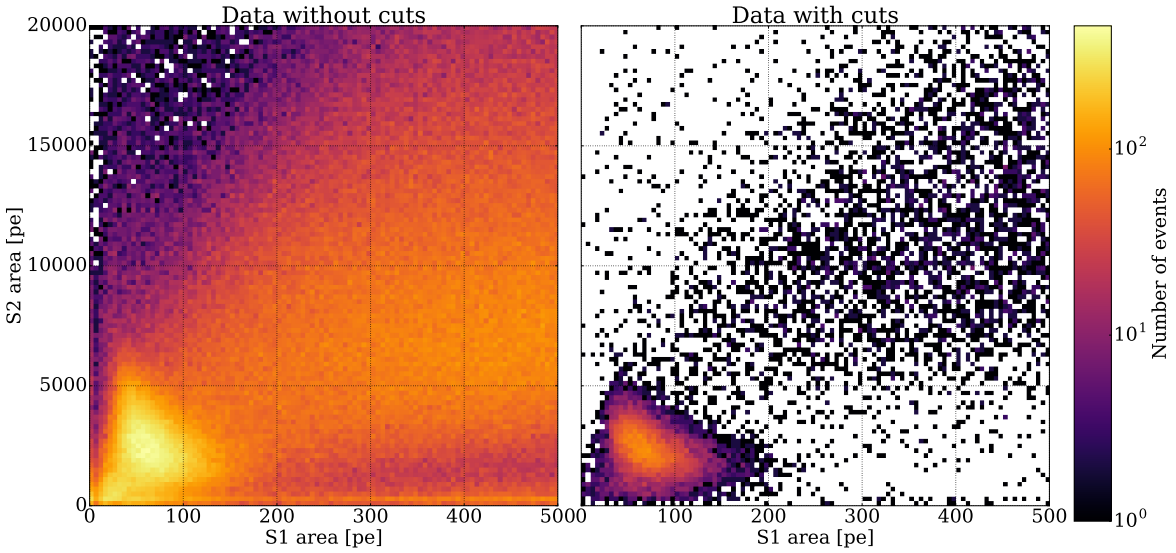

Figure 4.11: Two dimensional histogram of the S1 and S2 area for the data with and without cuts. After the cuts, a defined population remains.

the free electrons being caught by impurities such as oxygen increases with increasing travel distance in the TPC, the expected S2 signal decreases with increasing depth of the event. This is a direct measurement of the xenon purity and can be quantified with an "electron lifetime" that can be determined form the S2 vs. z-position dependence.

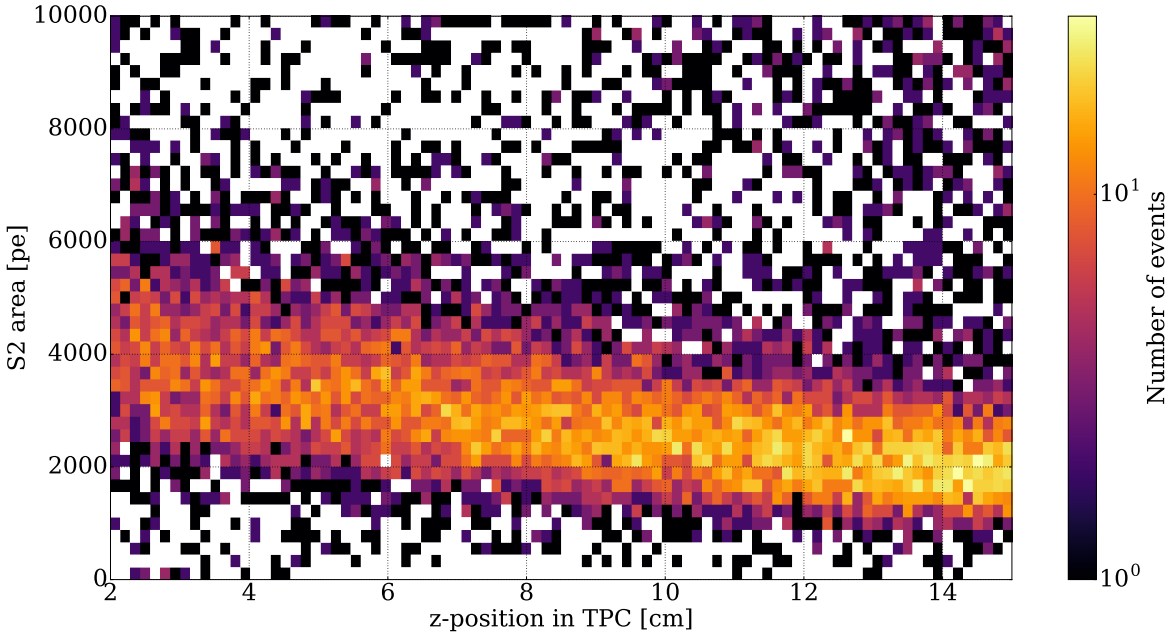

Figure 4.12: Two dimensional histogram of the S2 area and the z-position in the TPC. The area of the S2 signals decreases with increasing depth, which is caused by the limited lifetime of the free electrons.

However, before the electron life time is determined, it must be clearly shown that the observed population is caused by ^{83m}Kr. For this purpose, a background measurement without ^{83m}Kr in the detector must be compared with the data shown here.

5 Conclusion and outlook

In this bachelor thesis, measurements for the calibration and recommissioning of the Münster TPC were performed. This included the determination of the gain values for the photomultiplier tubes and the experimental identification of the optimal liquid level within the TPC.

First, the working principle of a TPC was explained. In addition, the design of a photomultiplier was described.

Based on several measurements with a UV-LED, the gain of each PMT was determined by convolution of the measured electrical noise with the expected spectrum. Since the pedestal peak led to a χ^2_ν that differed from one, the errors of the bins were manually changed to take the single and multiple photoelectron peaks more into account. It has been shown that the gain remains constant within the context of uncertainties, so that the originally defined values specified in table 3.1 could be used for processing of the raw data.

In the fourth part of the work, the liquid level of the xenon within the TPC was investigated. For this purpose, the calibration of the capacitance-based level meter was explained. Then measurements were performed at different liquid levels and examined with regard to the event rate and S2/S1 area ratio. It has been found that both values strongly depend on the liquid level and the optimum level is $205.2 \pm 2.3\,\mathrm{mm}$. However, there was a difficulty with the level meter calibration, which could have been caused by a too early cooling of the temperature sensor. As a result, the determined filling heights indicate a liquid gas interface which would be above the anode and no more S2 signals would be expected to occur. This is in contrast to the observations made.

The width of the zone with high S2 rate was determined to be 4.73 mm which is in agreement with the expectation of 5 mm from the gate to anode distance. Furthermore, it has been shown that the S2/S1 ratio also varies considerably in the area between the gate and the anode. A precise adjustment of the liquid level is therefore necessary. This can be done by the evaluation of the most frequent S2/S1 area ratio.

Now that the optimal level has been found, it was finally examined whether the events produced by ^{83m}Kr decay can be identified. For this purpose two cuts have been defined. ^{83m}Kr events were selected according to their z-position and the occurrence of two S1 signals

form the subsequent decays in a given time window. It turned out that a specific population in the S1-S2 area histogram remains. This is a clear indication of ^{83m}Kr. Further confirmation can be achieved in the future by a background measurement without injection of ^{83m}Kr. In this measurement, the observed population should disappear when applying the same cuts. Another possibility is to stop the ^{83m}Kr supply during a measurement and check if the population decreases with the appropriate half-life according to the decay law.

The combination of plausible PMT gain values and the optimum liquid level now allows for a number of further investigations. The procedure for determining the electron lifetime has already been briefly described. If this is known, the S2 signals can be corrected depending on their origin. Furthermore, after the identification of a homogeneously distributed monoenergetic source such as ^{83m}Kr, the S1 signals can also be corrected depending on their position since the efficiency for photon detection is not uniform within the TPC due to geometric reasons. After these basic corrections have been determined an energy calibration can be performed. For this purpose, the detector is exposed to at least one other radioactive source with known energy. By identifying the corresponding peaks in the S1-S2 area histogram, it is then possible to convert the measured S1 and S2 signal areas into energies. This will be done in the master thesis of K. Gauda.

6 Appendix

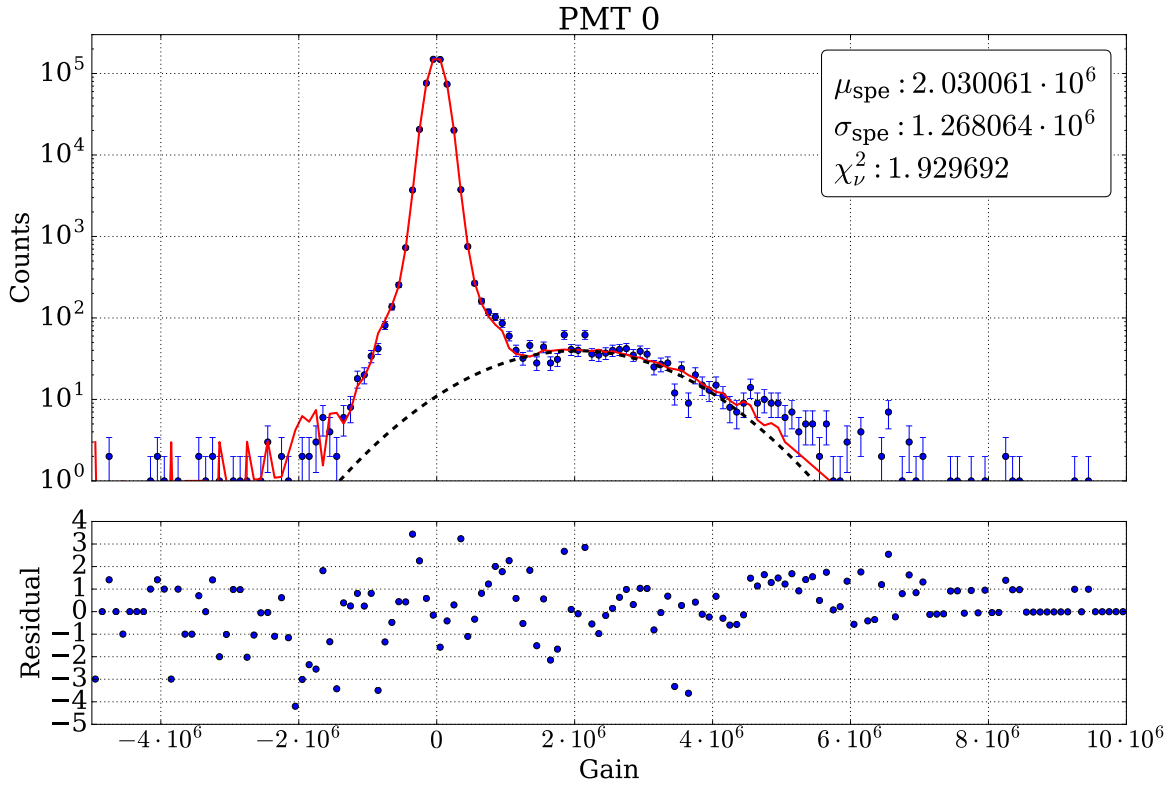

Figure 6.1: Fit for PMT 0

$$\Delta\mu_{(\text{rel. dev})} = \sqrt{\left(\frac{\mu_{\max} - \mu}{\mu \cdot |\mu_{\max} - \mu|}\Delta\mu_{\max}\right)^2 + \left(\frac{\mu_{\max}(\mu_{\max} - \mu)}{\mu^2 \cdot |\mu_{\max} - \mu|}\Delta\mu\right)^2} \tag{6.1}$$

$$\Delta f = \sqrt{\left(\frac{b - y}{a^2} \cdot \Delta a\right)^2 + \left(\frac{\Delta y}{a}\right)^2 + \left(\frac{\Delta b}{a}\right)^2} \tag{6.2}$$

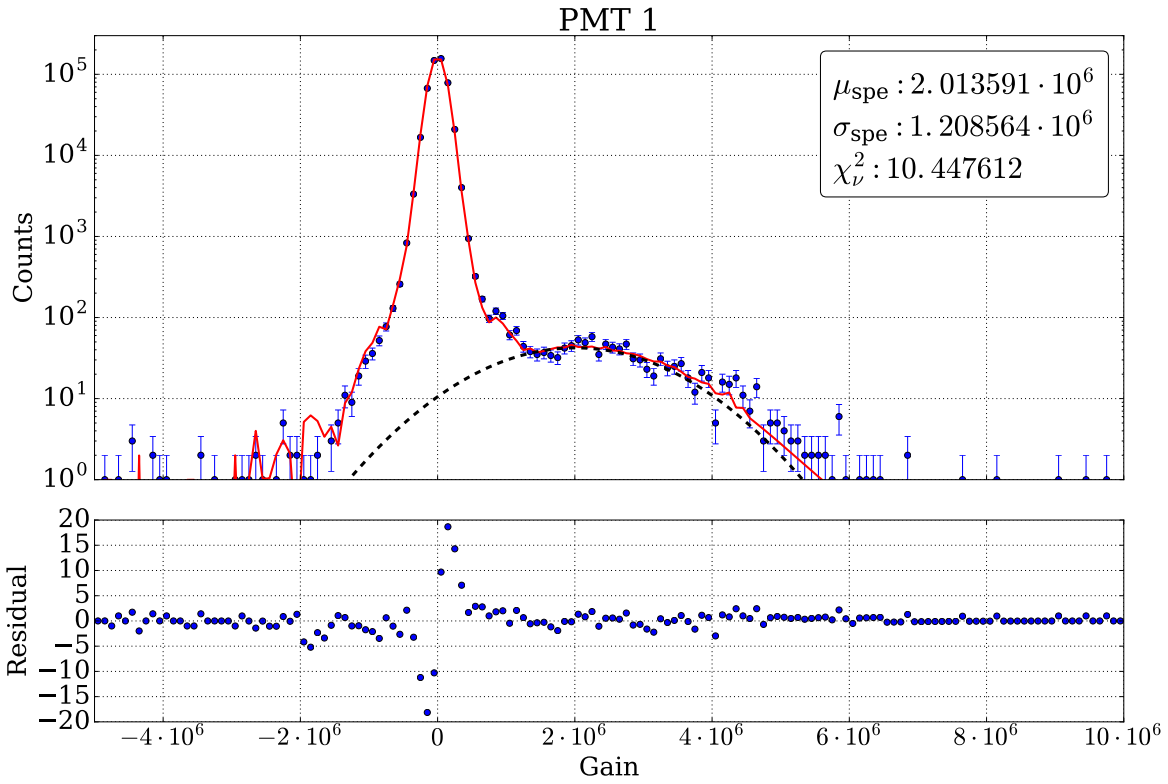

Figure 6.2: Fit for PMT 1

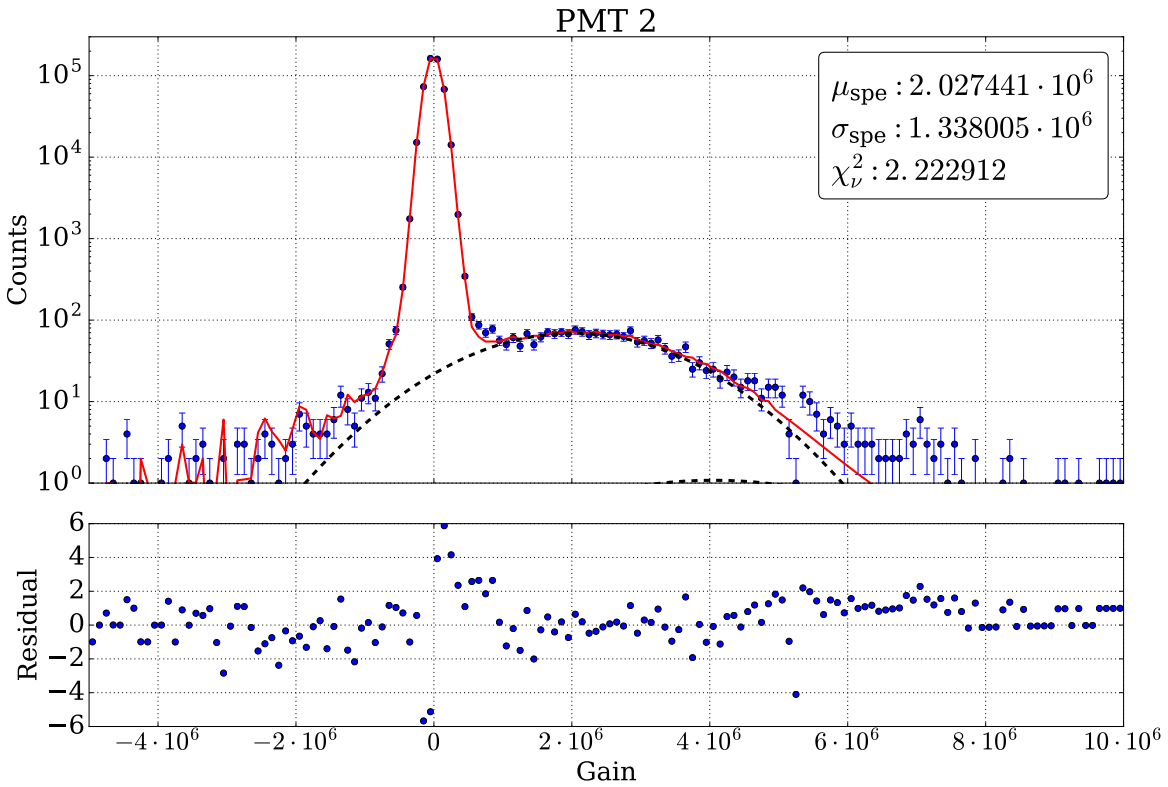

Figure 6.3: Fit for PMT 2

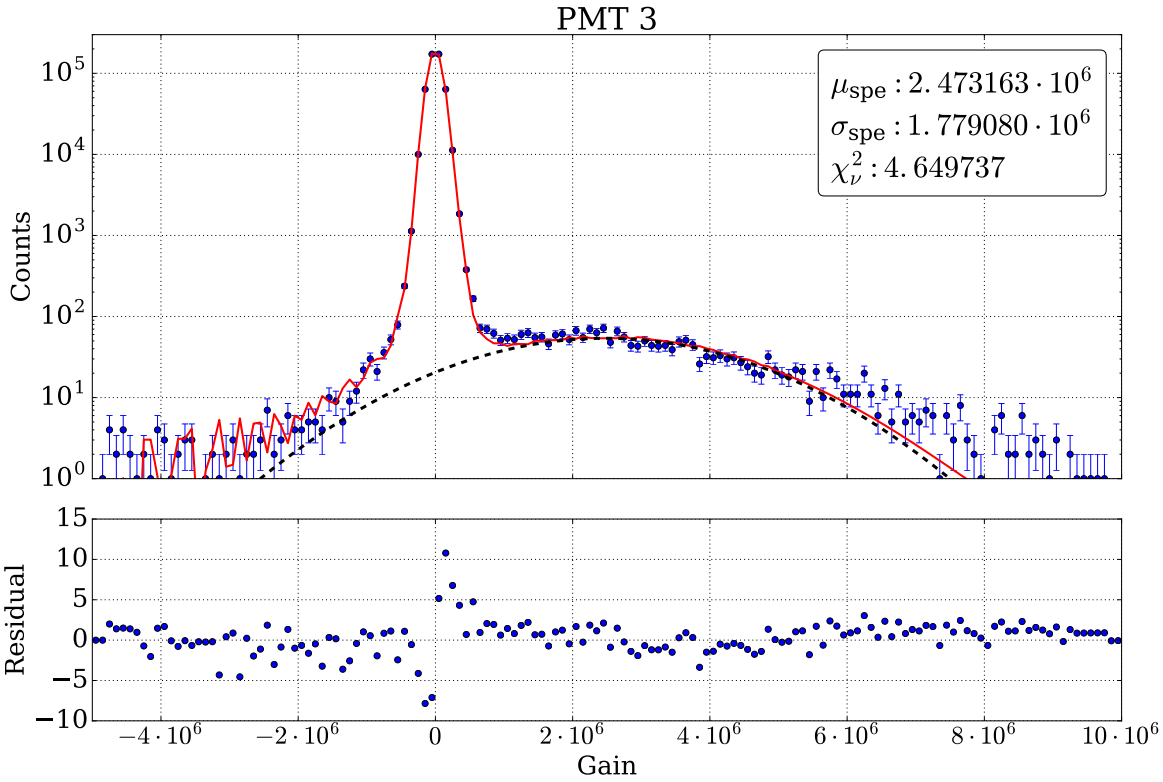

Figure 6.4: Fit for PMT 3

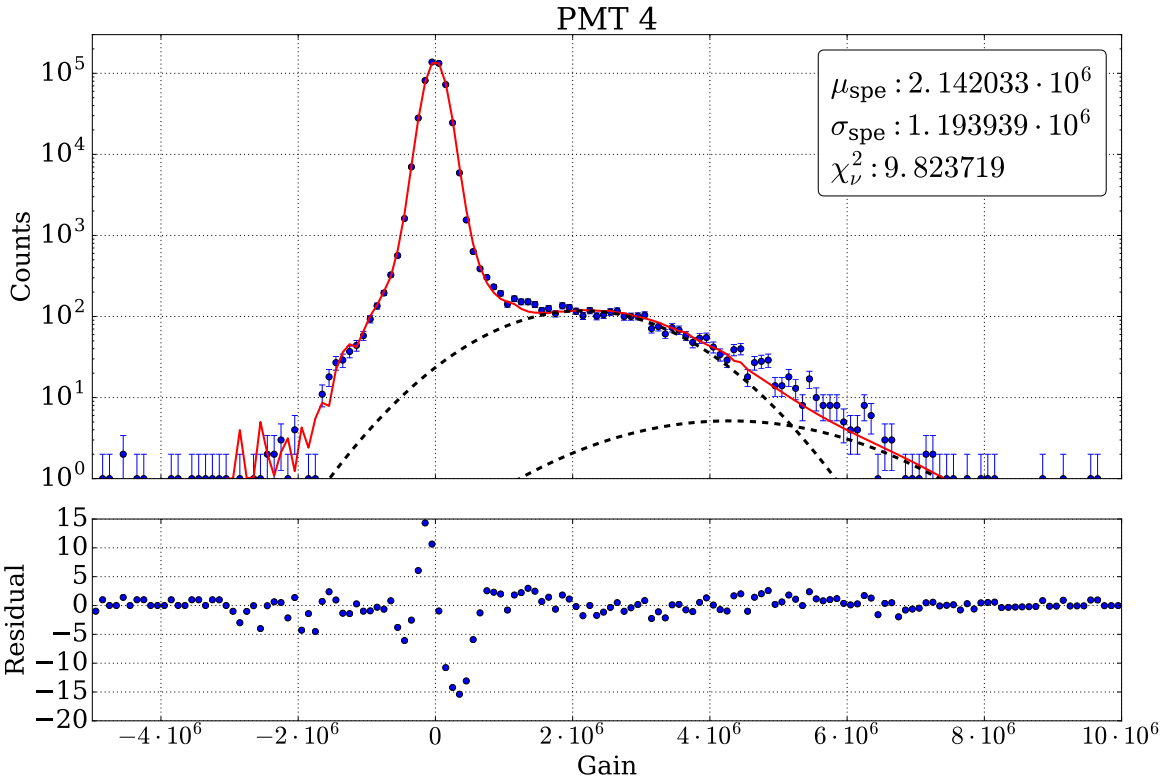

Figure 6.5: Fit for PMT 4

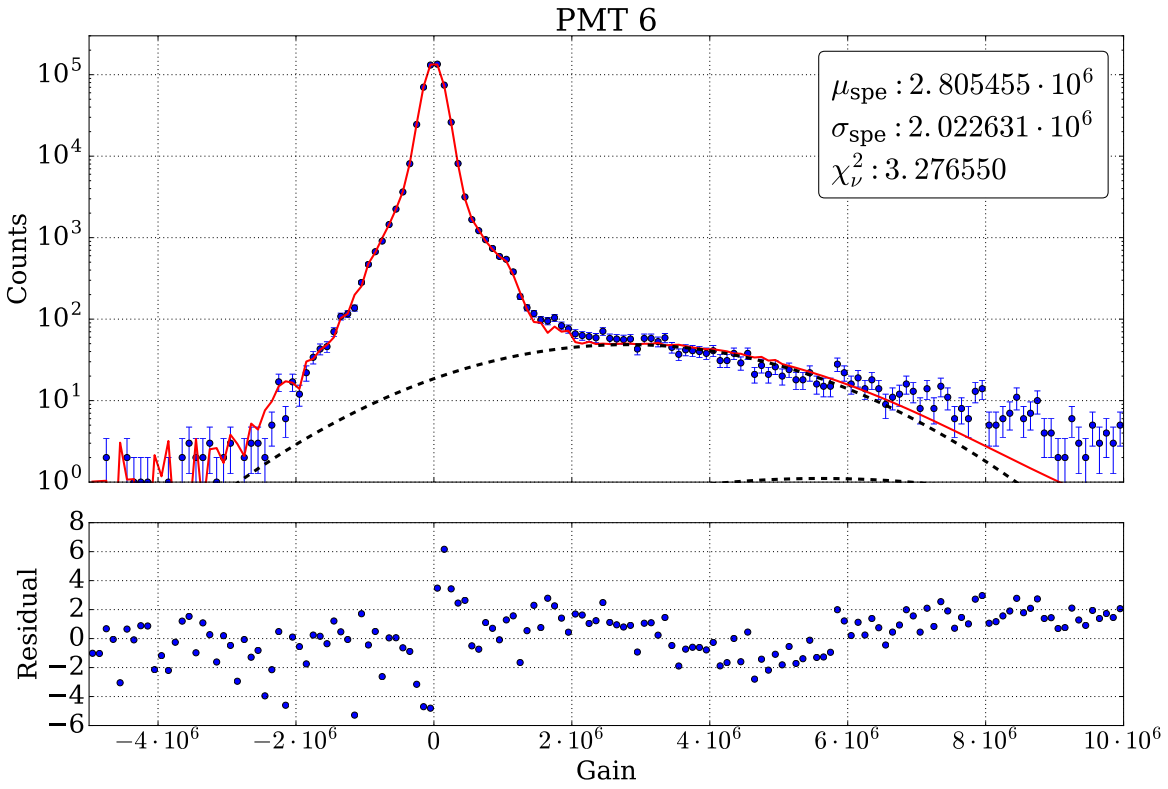

Figure 6.6: Fit for PMT 6

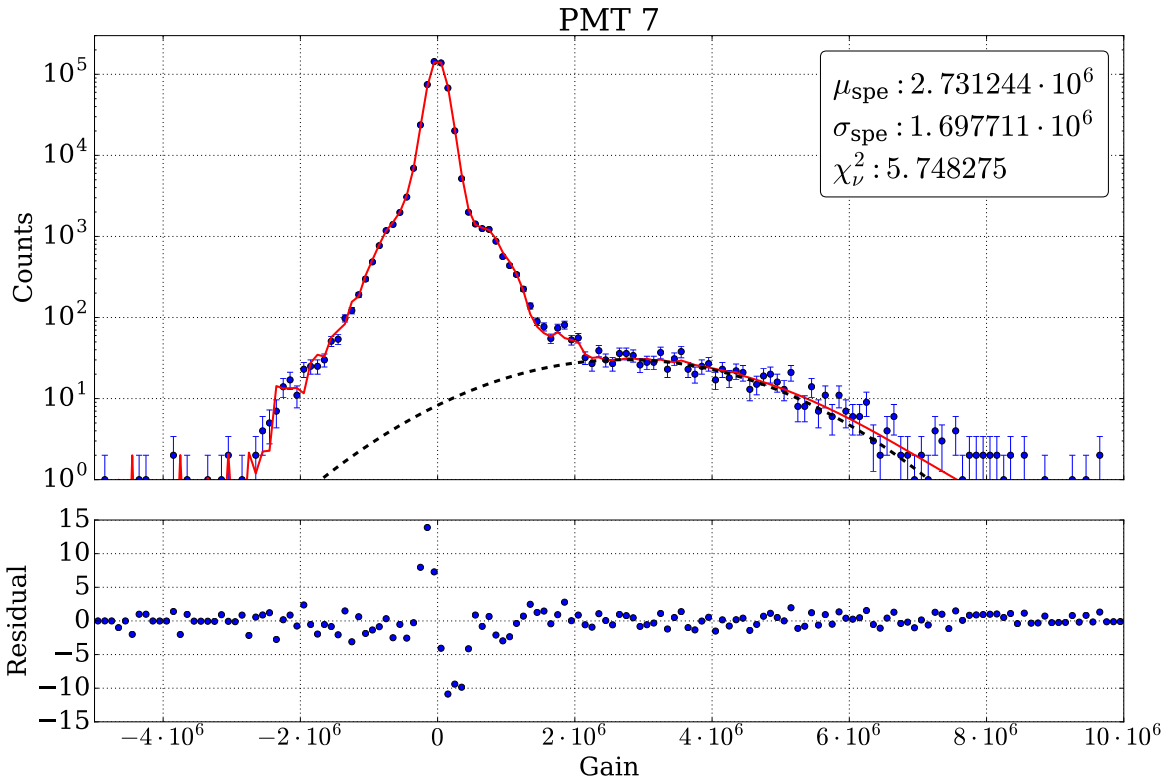

Figure 6.7: Fit for PMT 7

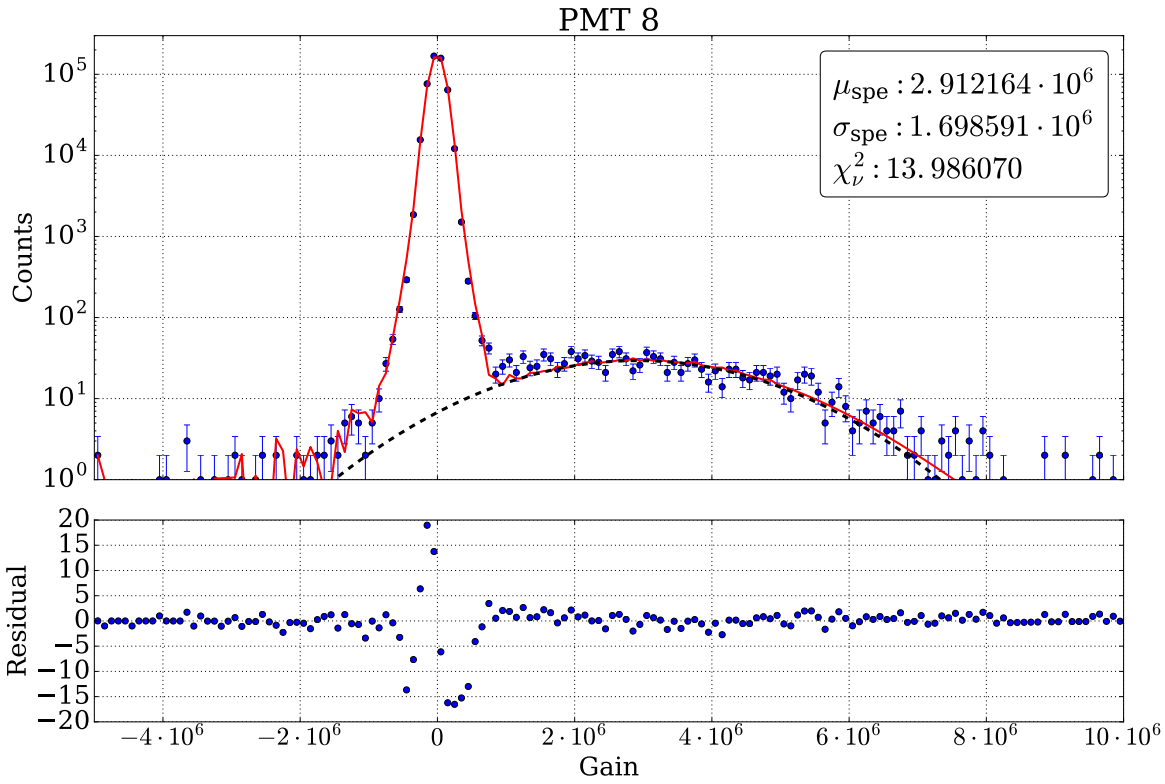

Figure 6.8: Fit for PMT 8

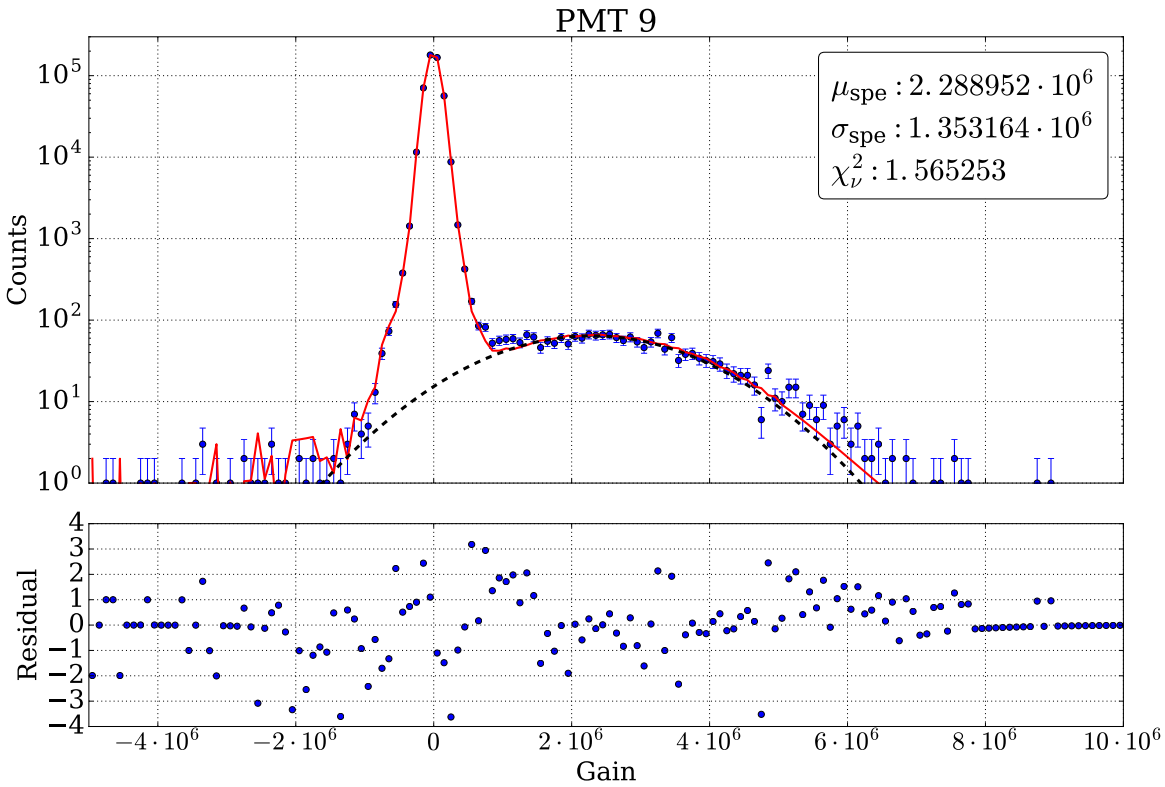

Figure 6.9: Fit for PMT 9

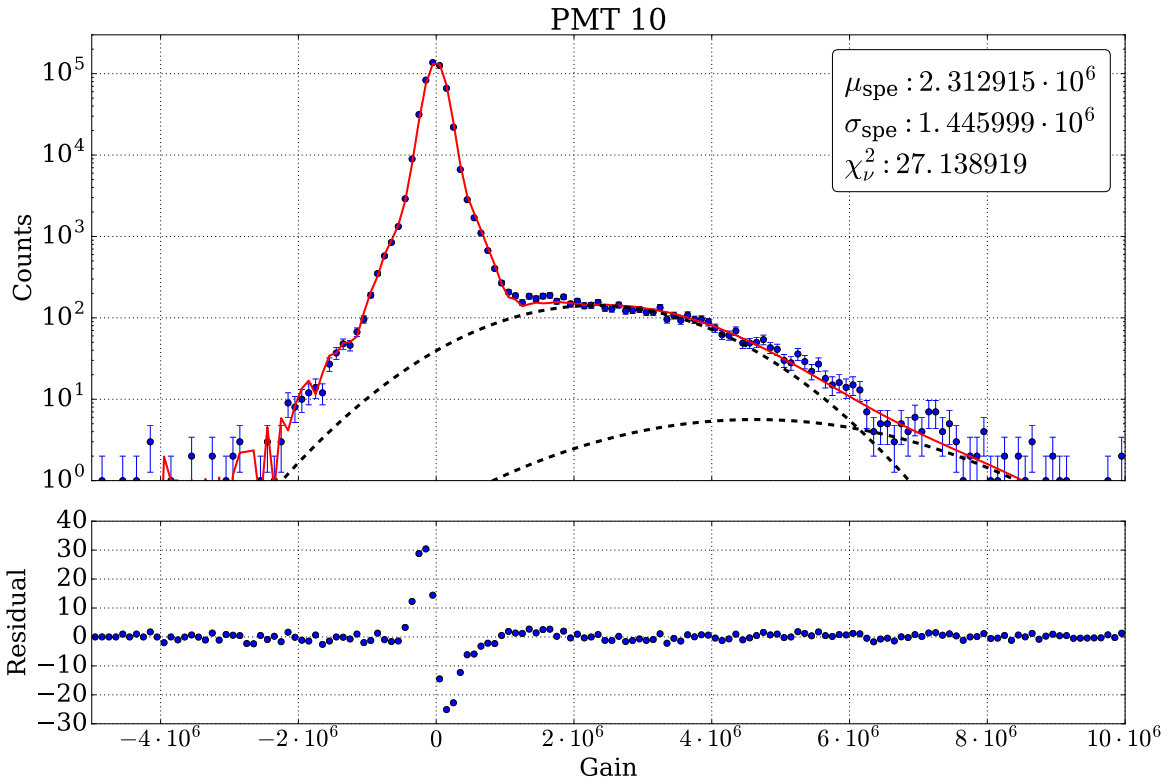

Figure 6.10: Fit for PMT 10

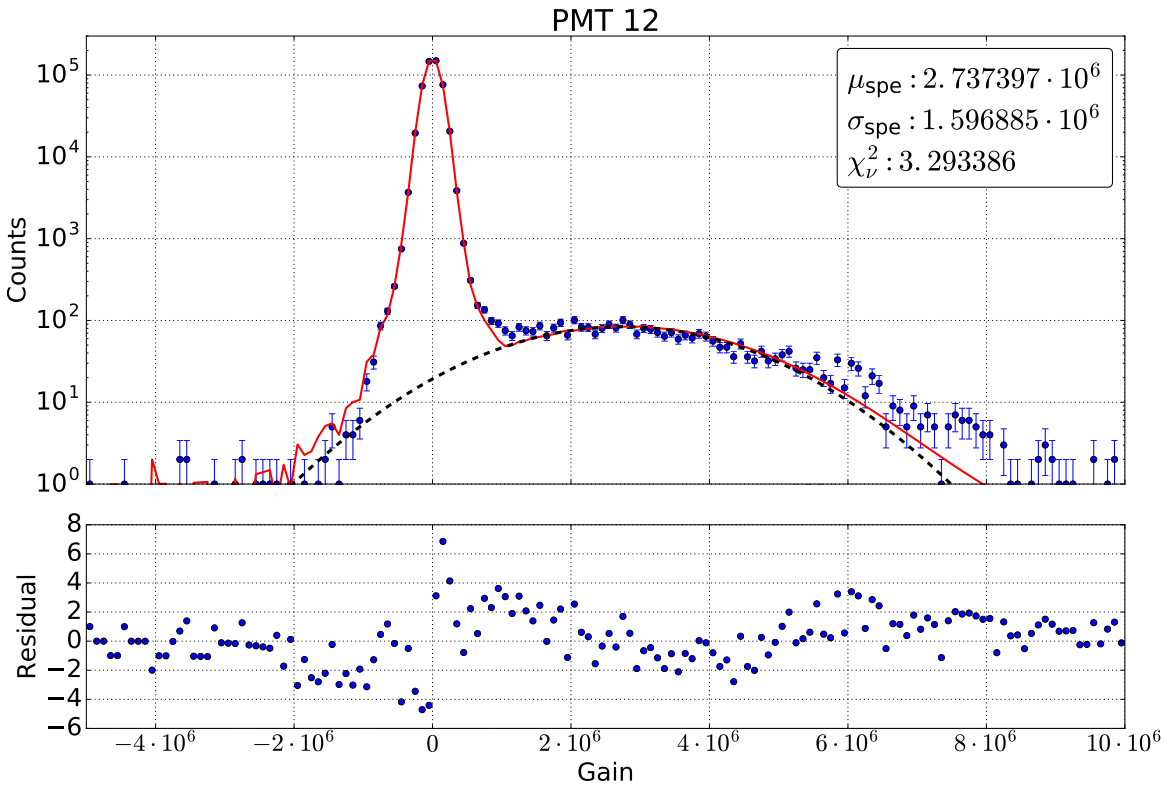

Figure 6.11: Fit for PMT 12

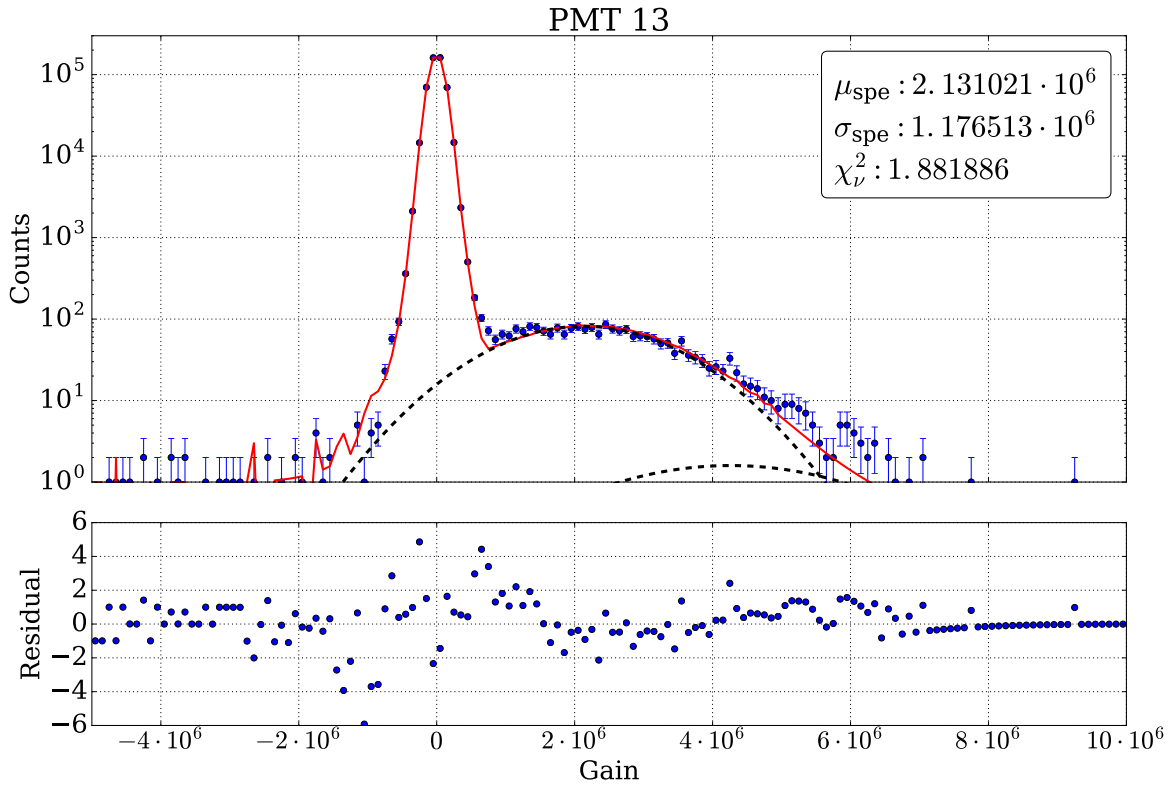

Figure 6.12: Fit for PMT 13

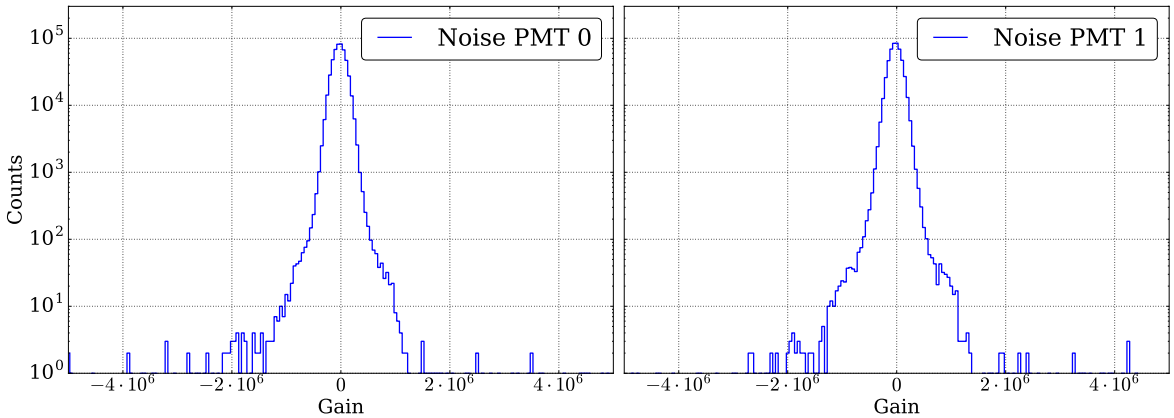

Figure 6.13: Measured electronic noise for PMTs 0 and 1.

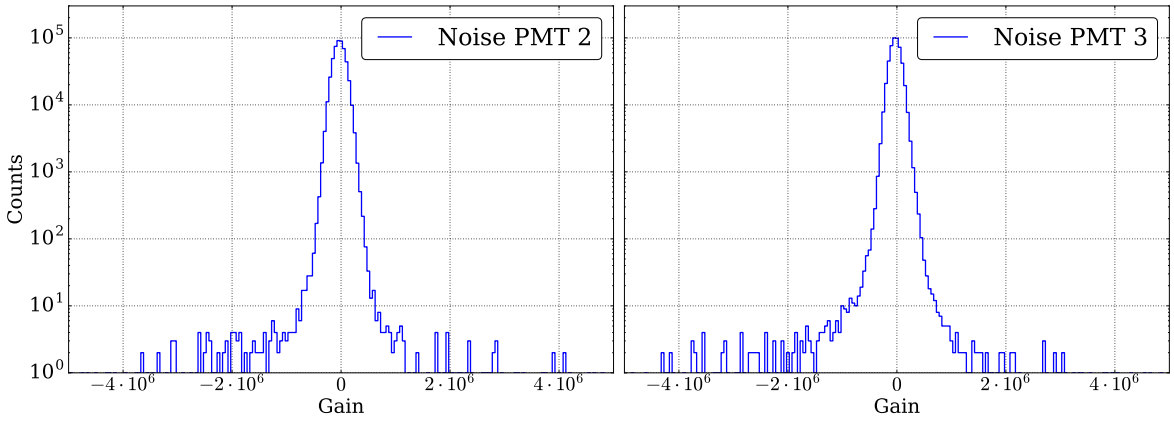

Figure 6.14: Measured electronic noise for PMTs 2 and 3.

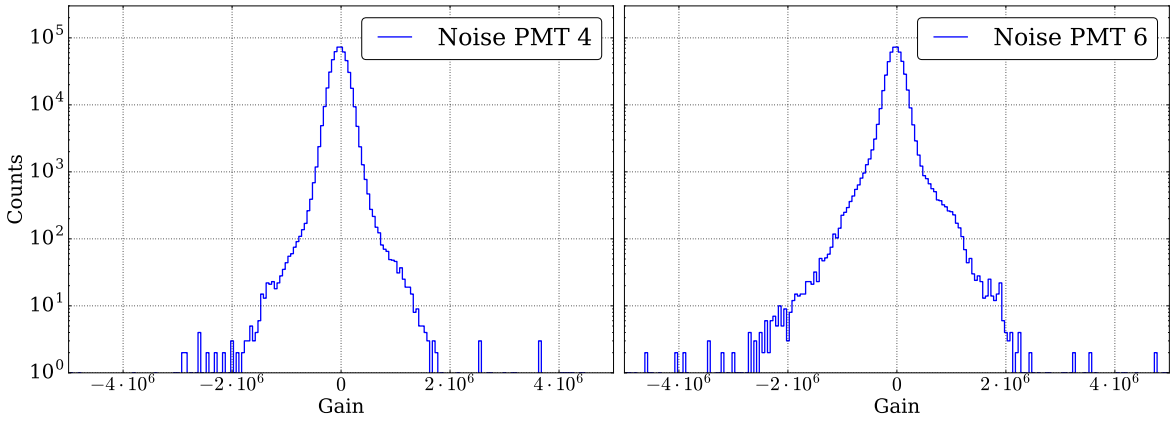

Figure 6.15: Measured electronic noise for PMTs 4 and 6.

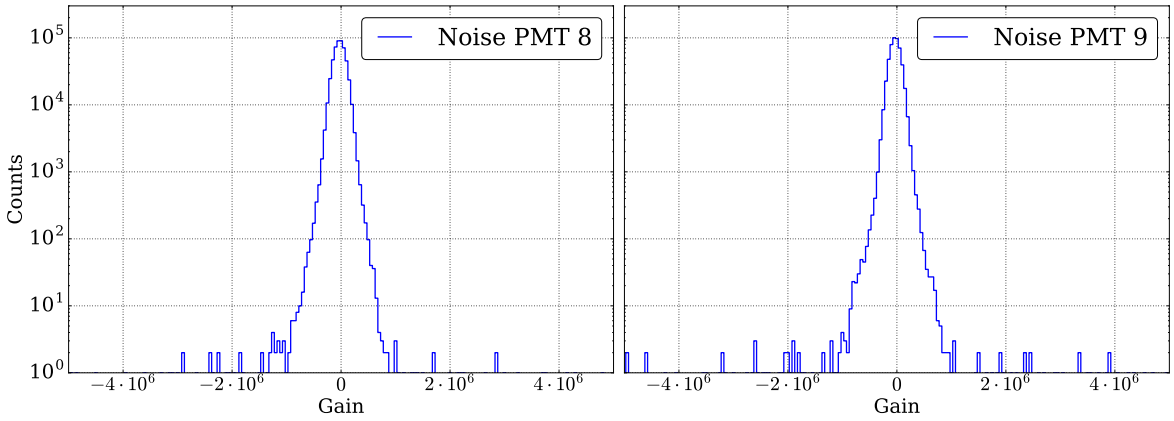

Figure 6.16: Measured electronic noise for PMTs 8 and 9.

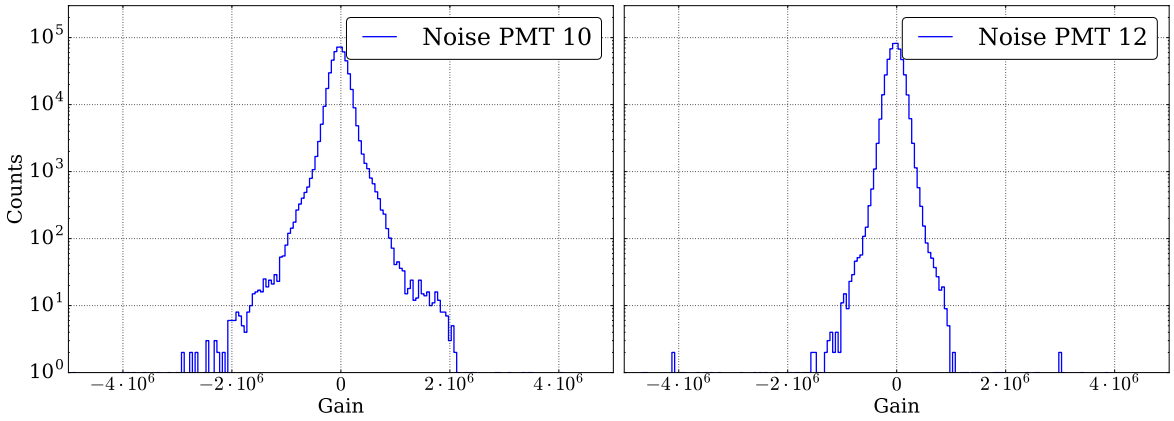

Figure 6.17: Measured electronic noise for PMTs 10 and 12.

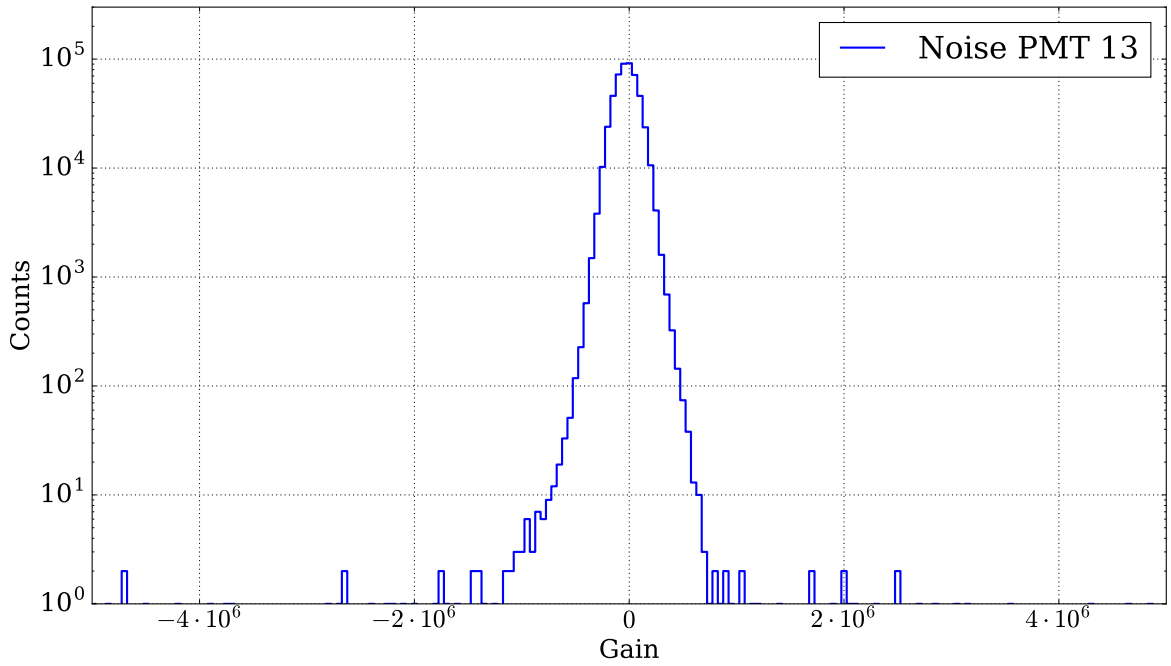

Figure 6.18: Measured electronic noise for PMTs 13.

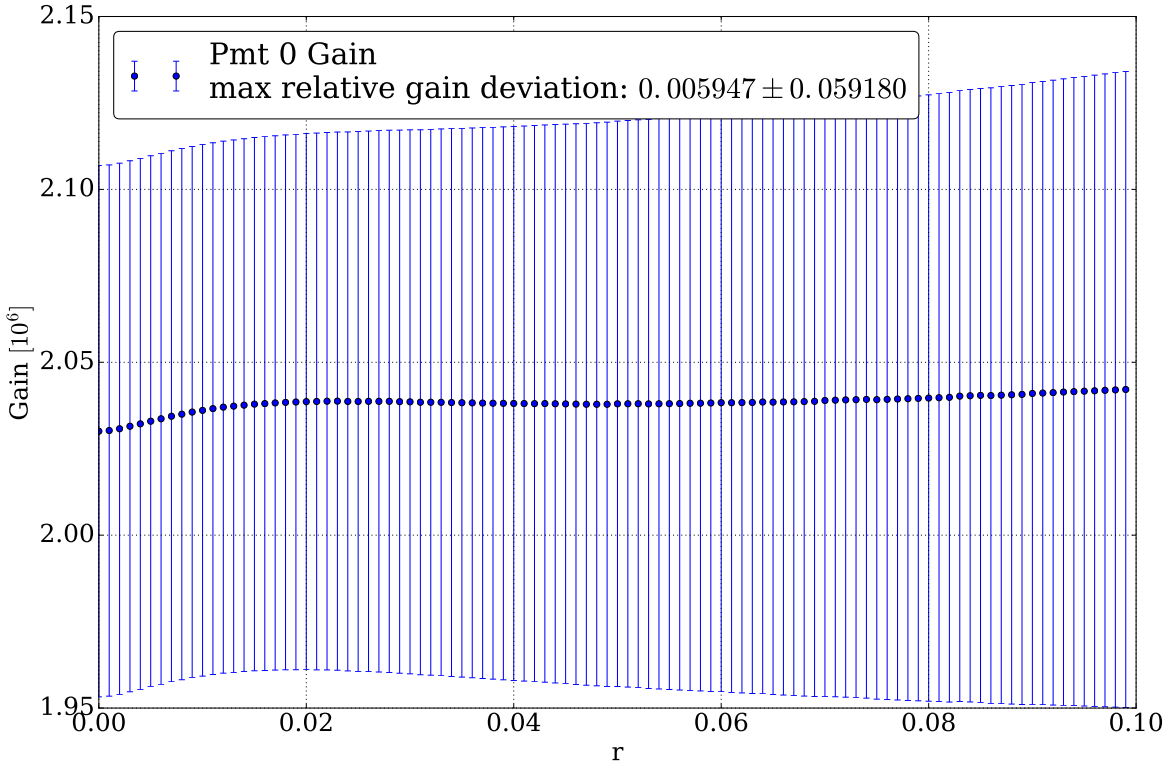

Figure 6.19: Result of the gain determination of PMT 0 plotted against r.

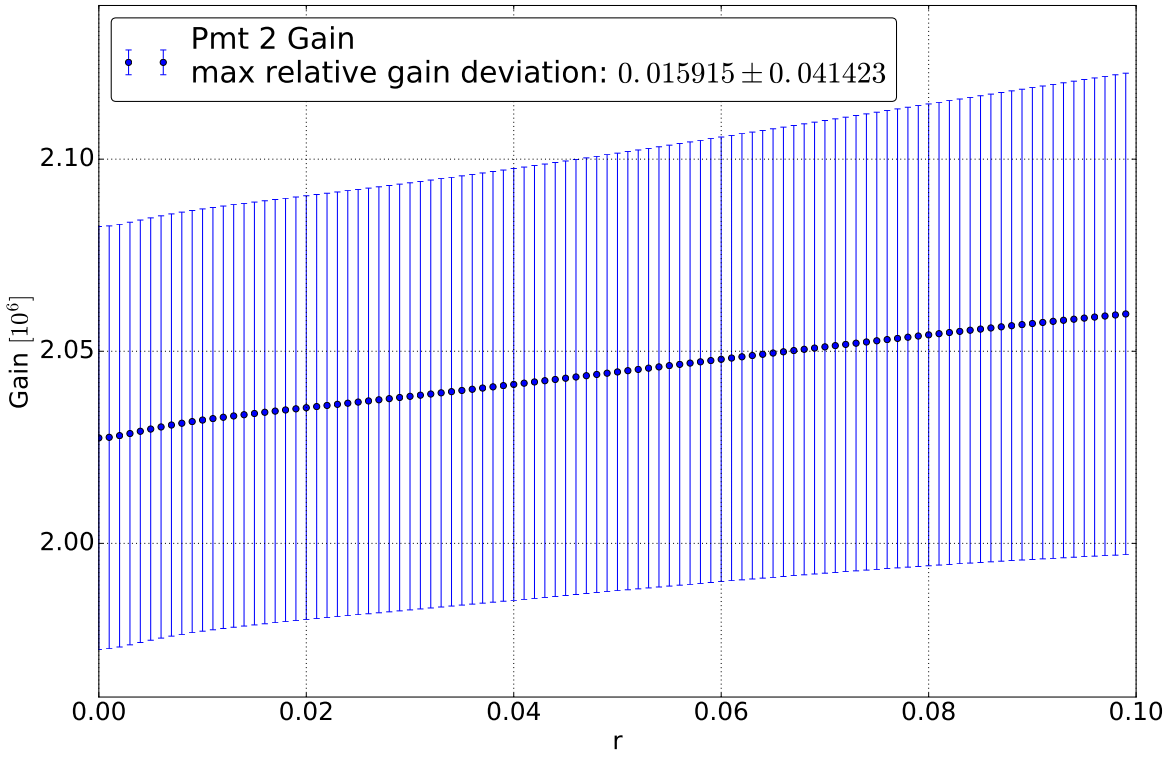

Figure 6.20: Result of the gain determination of PMT 2 plotted against r.

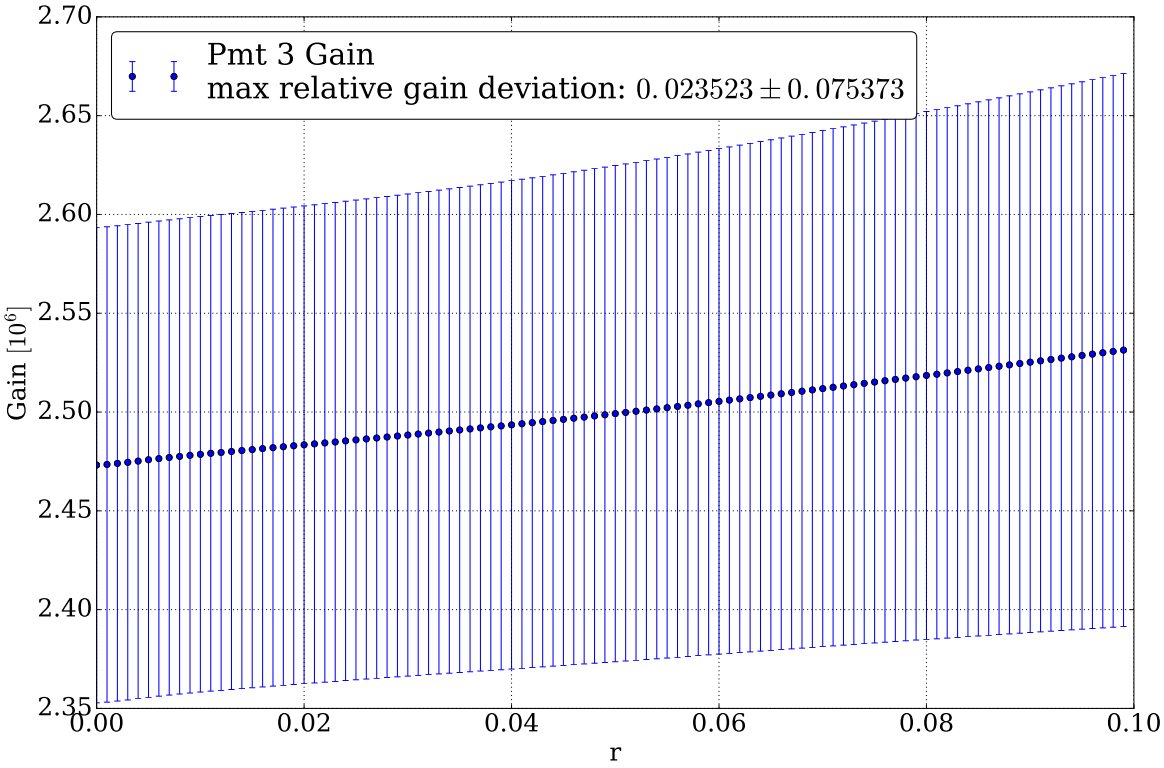

Figure 6.21: Result of the gain determination of PMT 3 plotted against r.

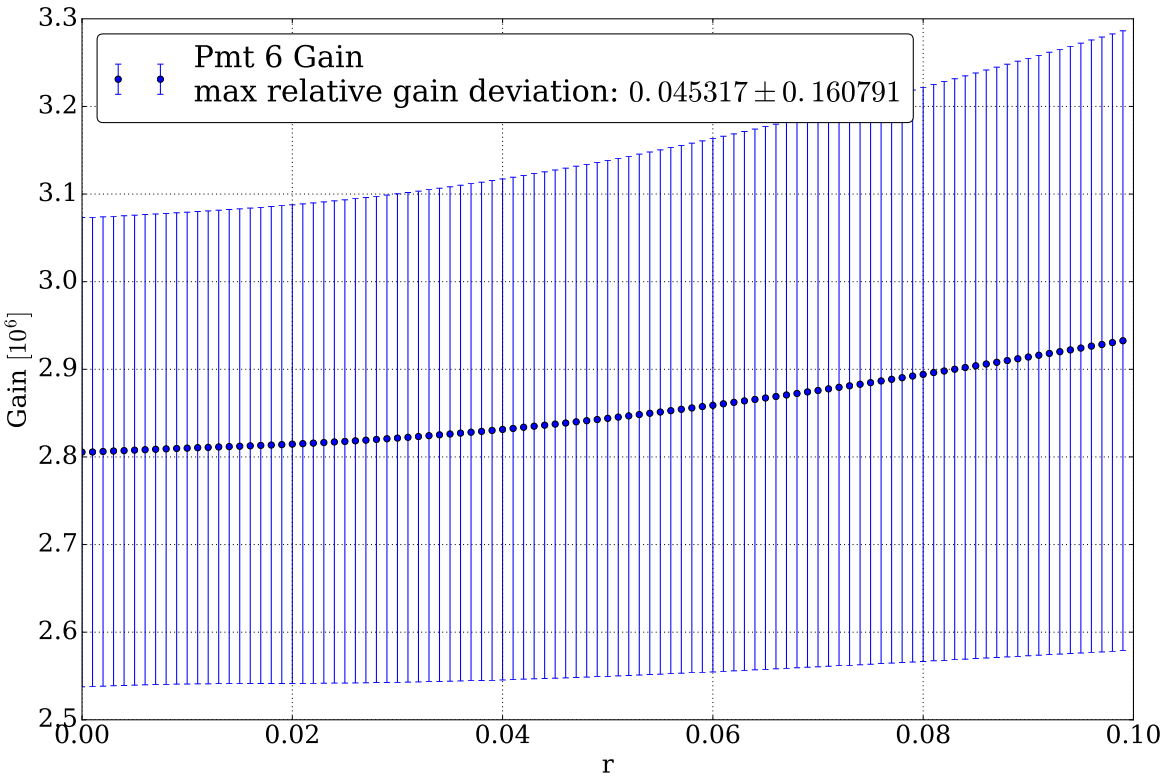

Figure 6.22: Result of the gain determination of PMT 6 plotted against r.

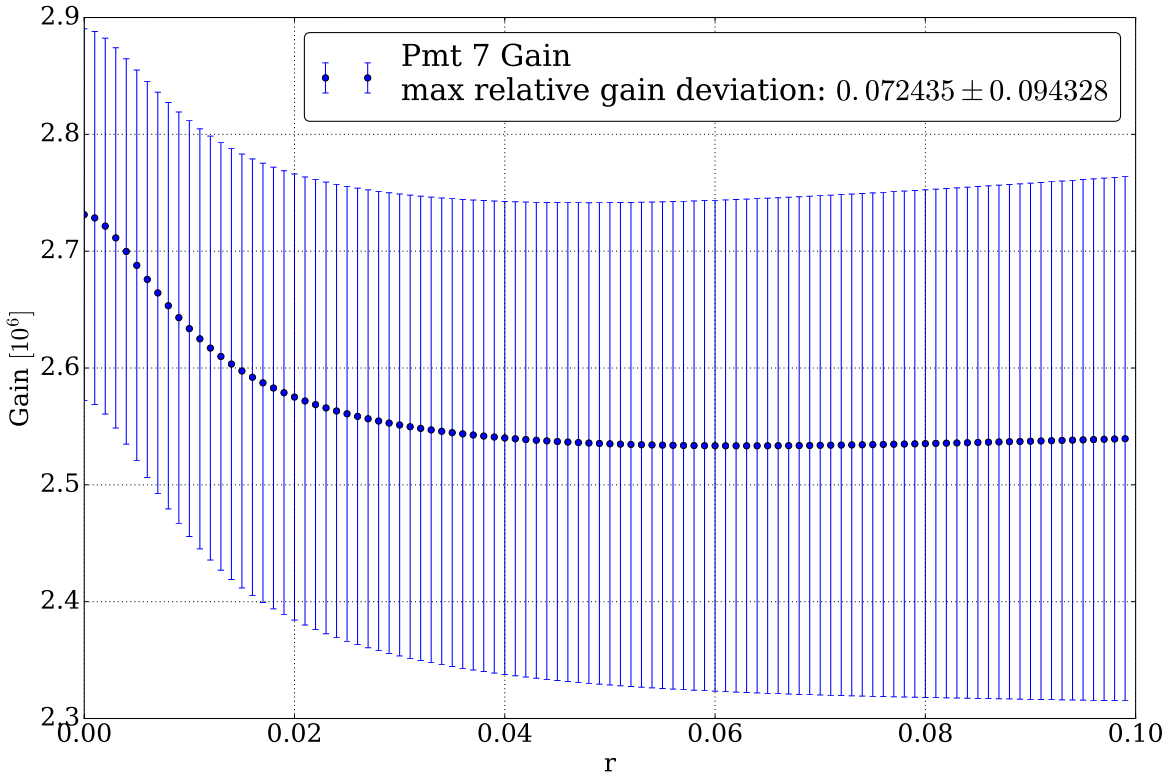

Figure 6.23: Result of the gain determination of PMT 7 plotted against r.

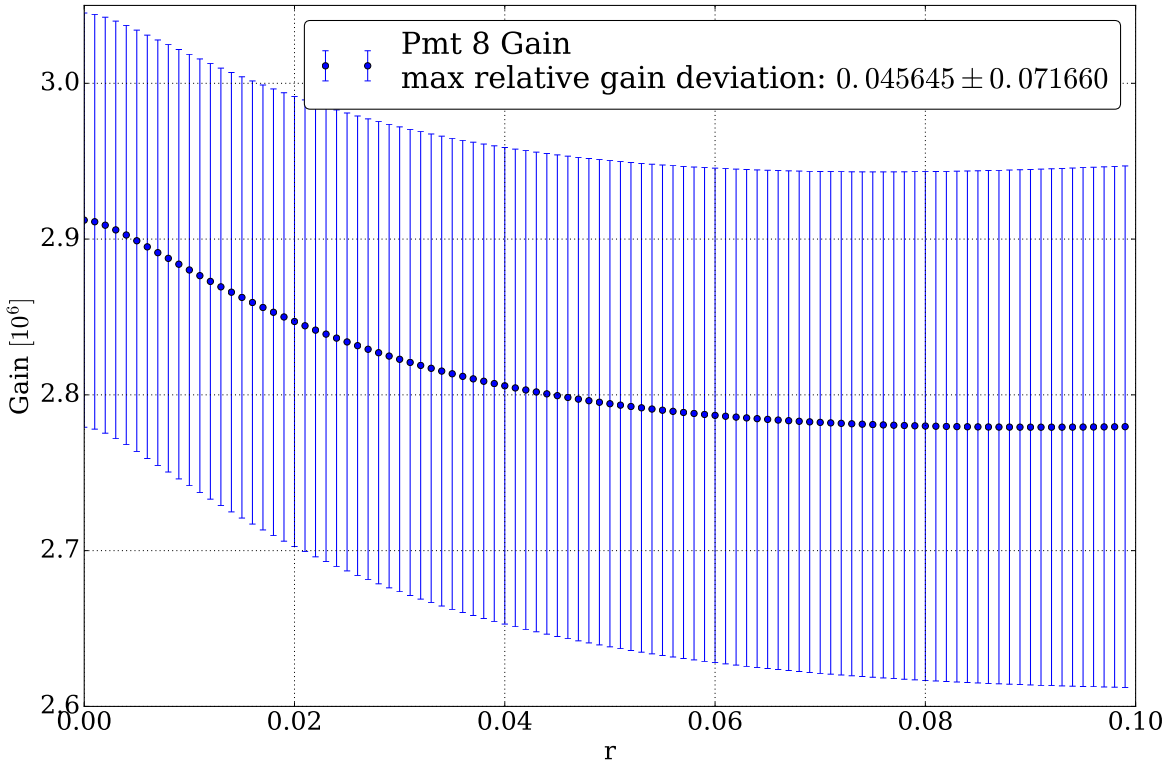

Figure 6.24: Result of the gain determination of PMT 8 plotted against r.

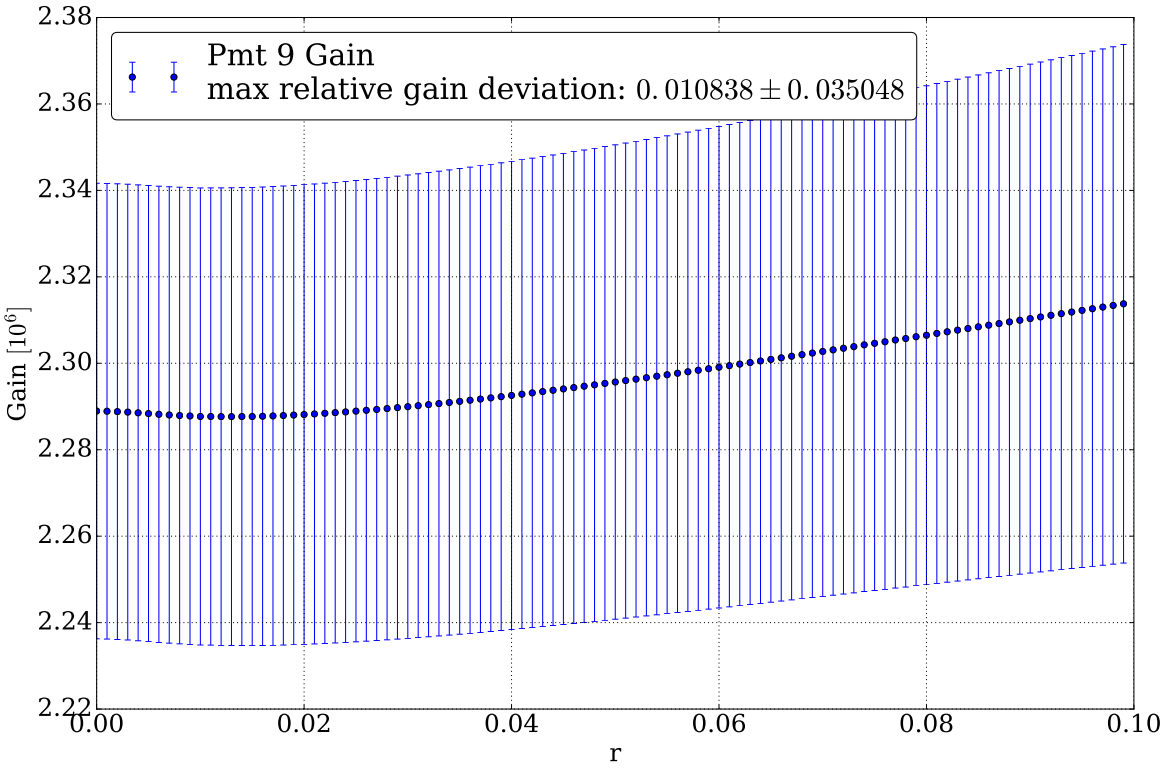

Figure 6.25: Result of the gain determination of PMT 9 plotted against r.

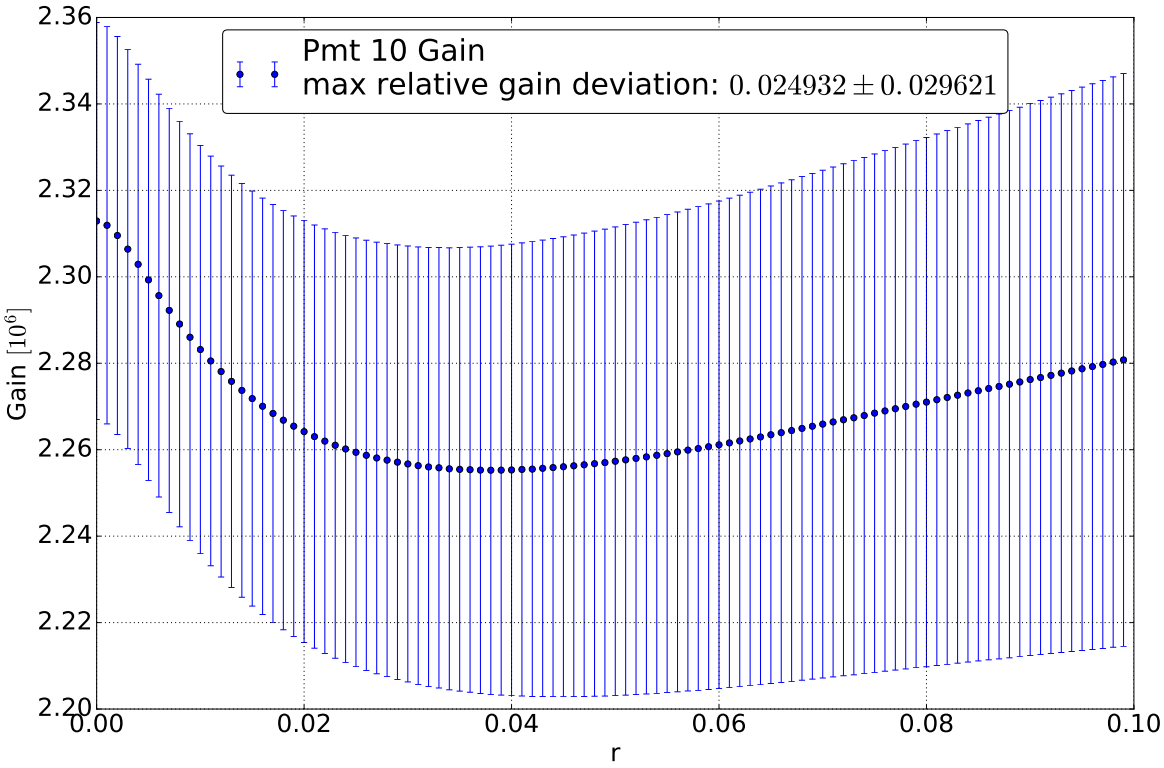

Figure 6.26: Result of the gain determination of PMT 10 plotted against r.

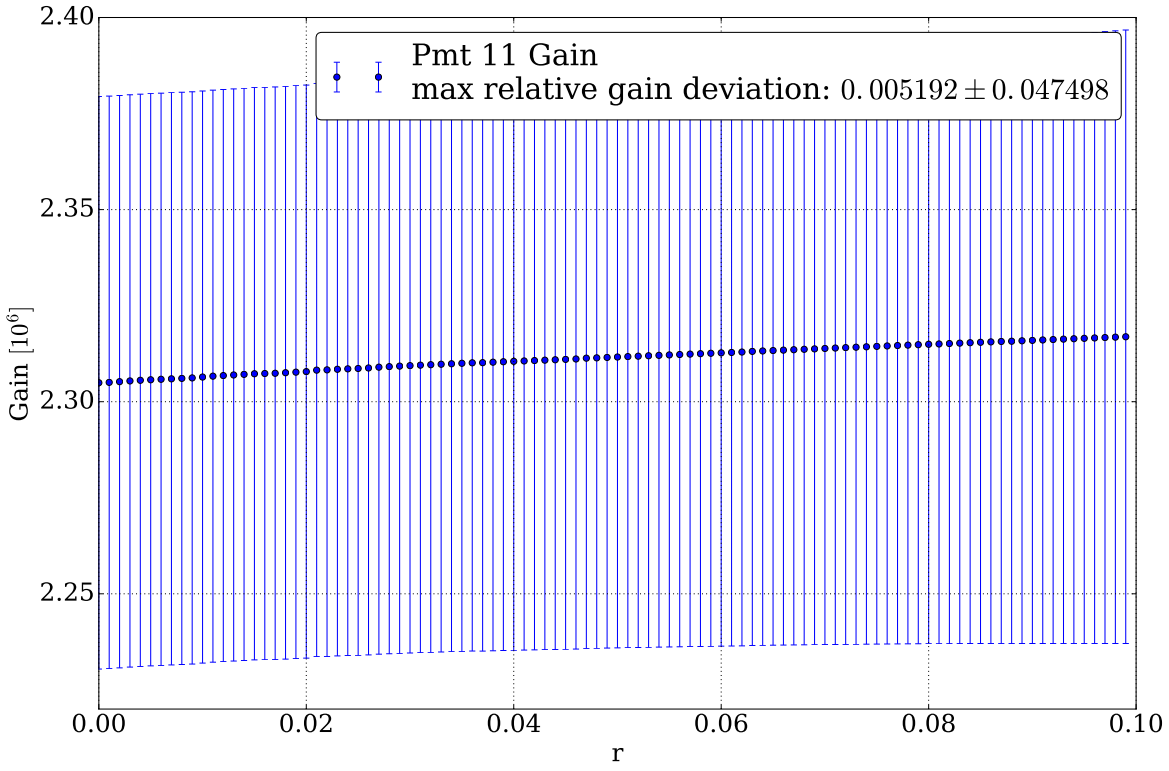

Figure 6.27: Result of the gain determination of PMT 11 plotted against r.

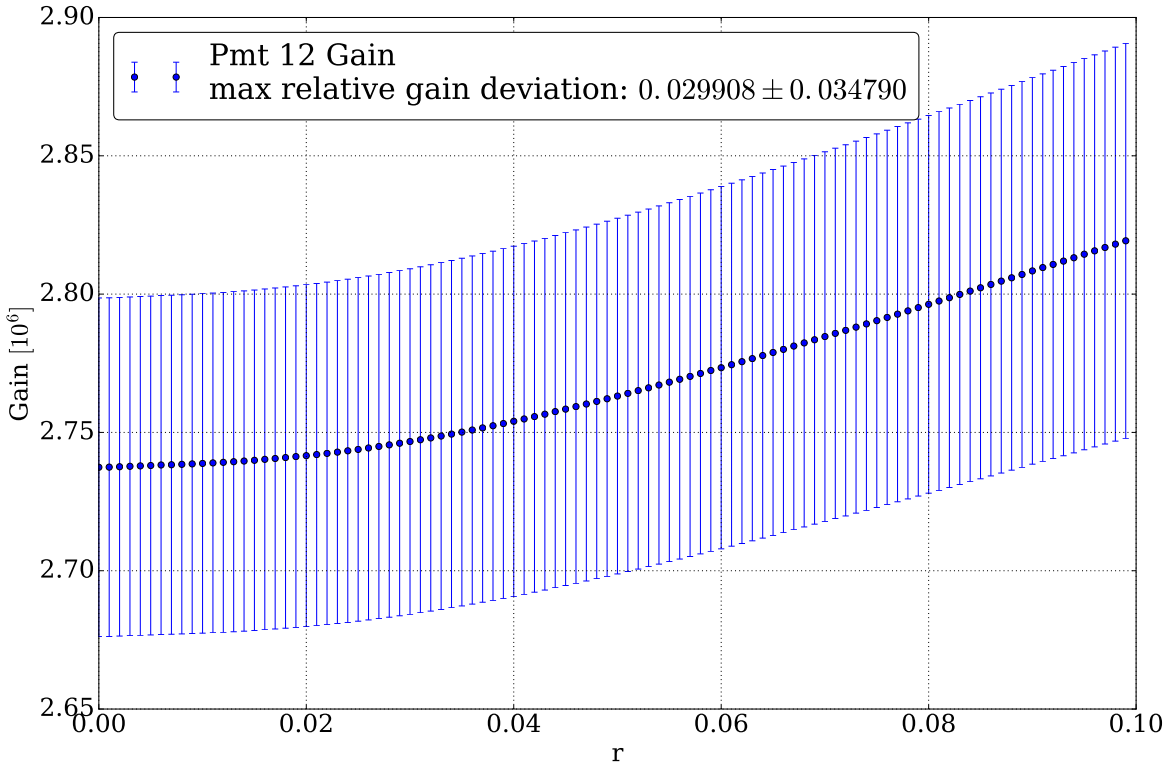

Figure 6.28: Result of the gain determination of PMT 12 plotted against r.

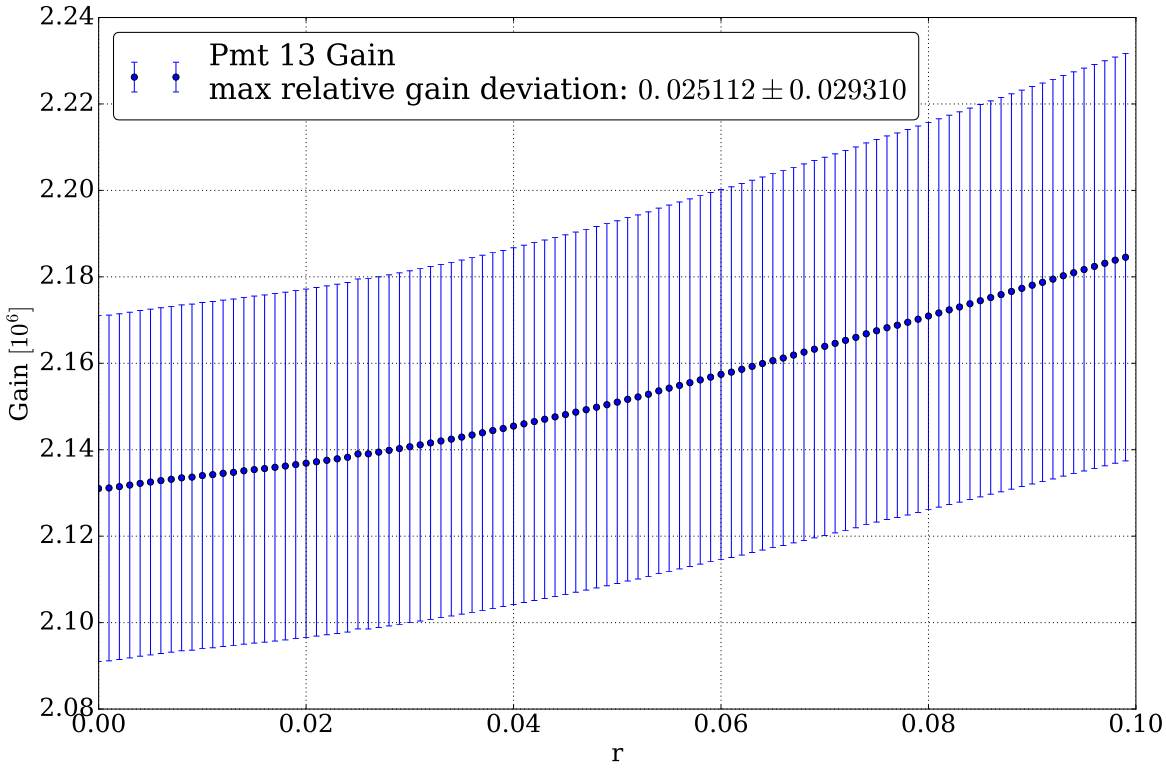

Figure 6.29: Result of the gain determination of PMT 13 plotted against r.

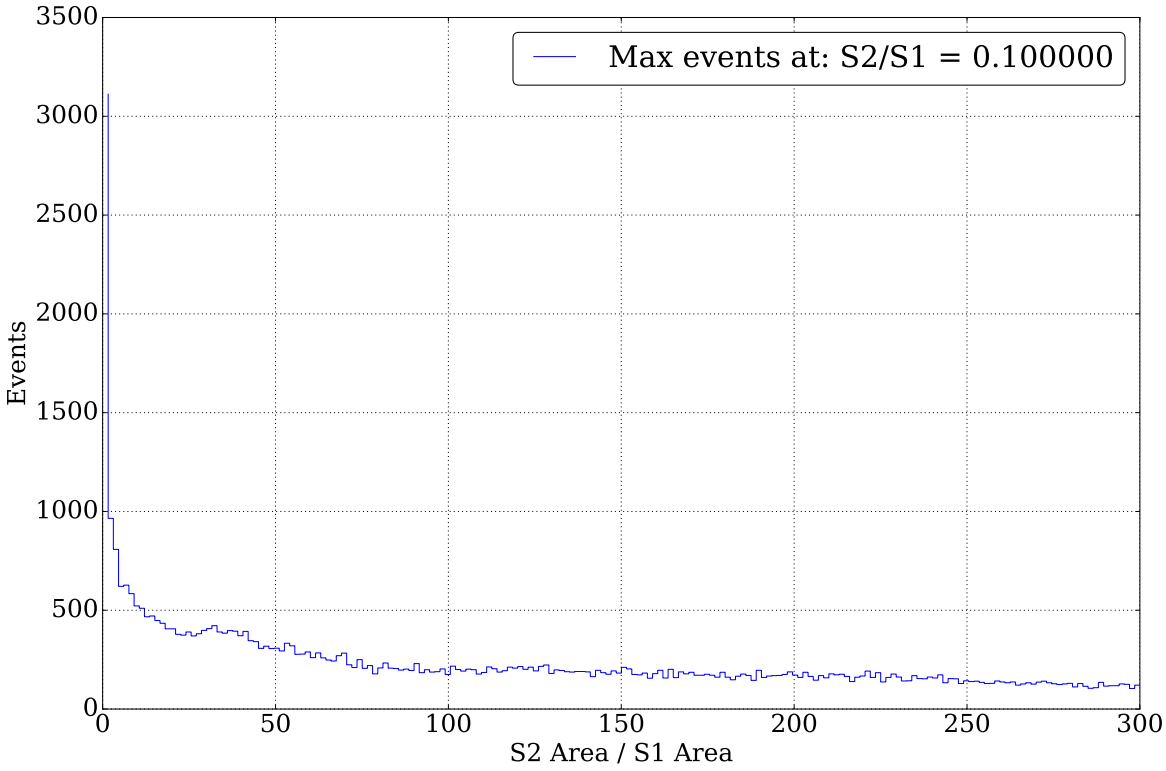

Figure 6.30: Histogram of the S2 Area S1 Area ratio for measurement 1.

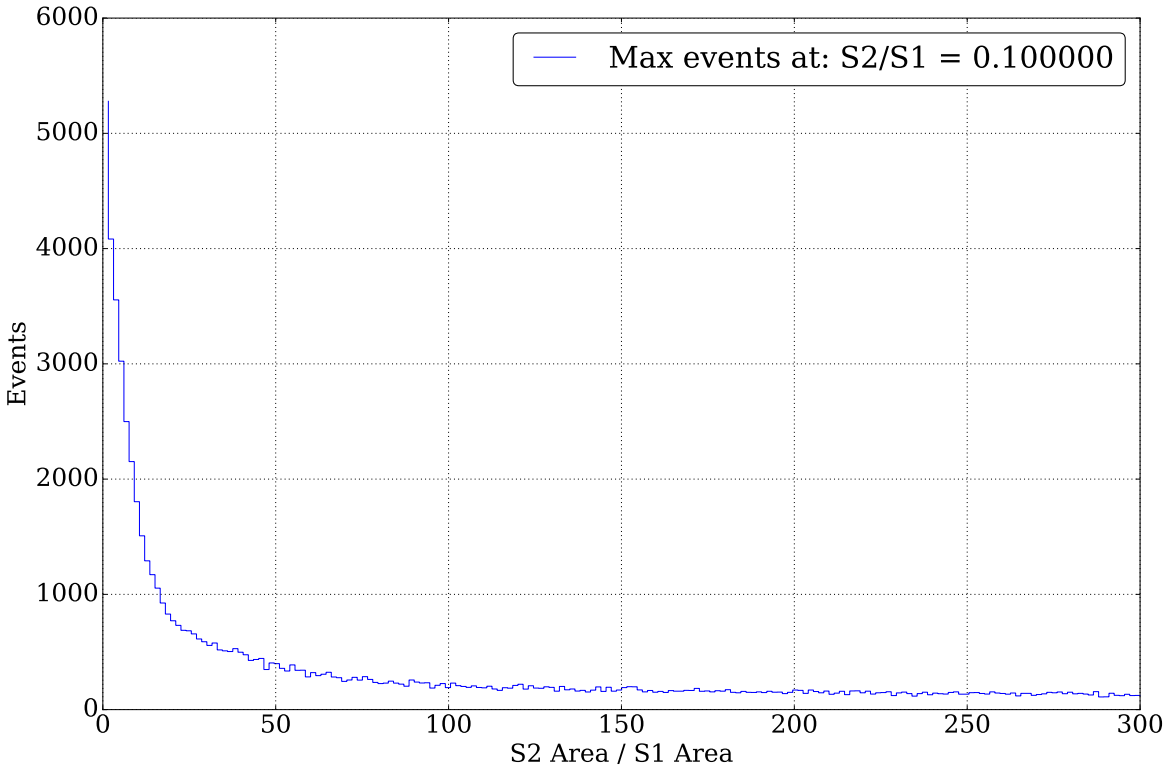

Figure 6.31: Histogram of the S2 Area S1 Area ratio for measurement 2.

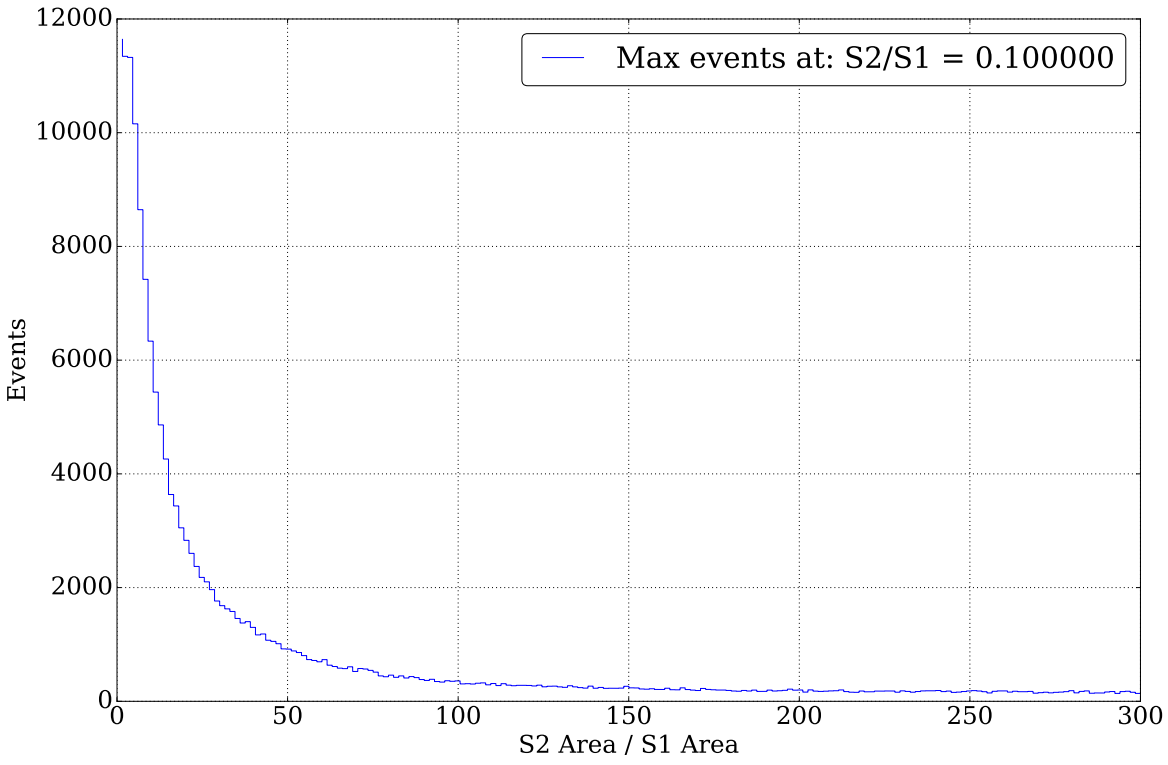

Figure 6.32: Histogram of the S2 Area S1 Area ratio for measurement 3.

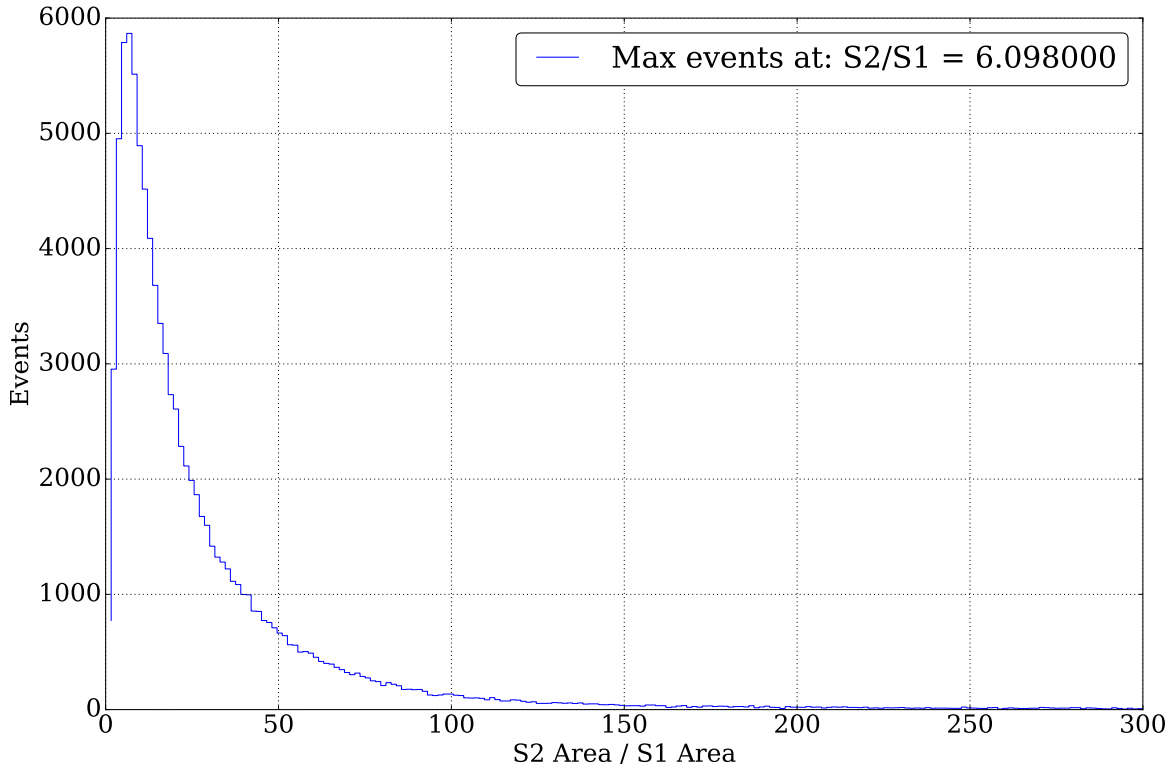

Figure 6.33: Histogram of the S2 Area S1 Area ratio for measurement 4.

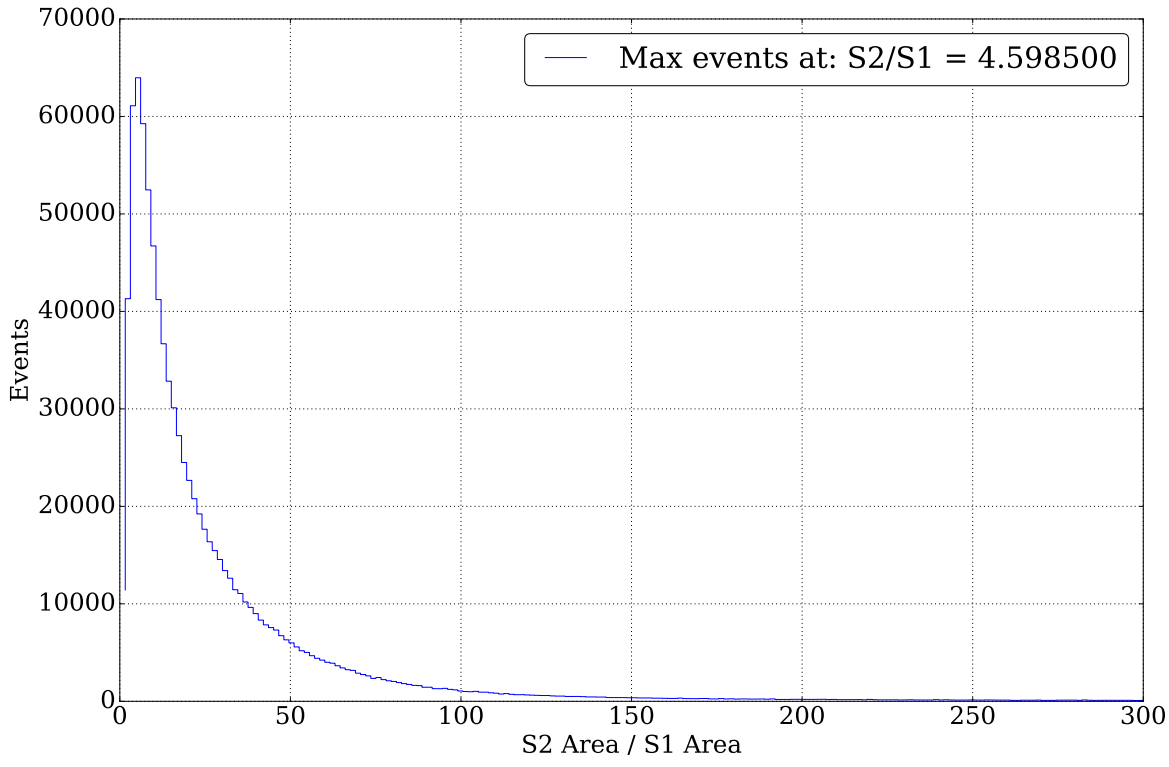

Figure 6.34: Histogram of the S2 Area S1 Area ratio for measurement 5.

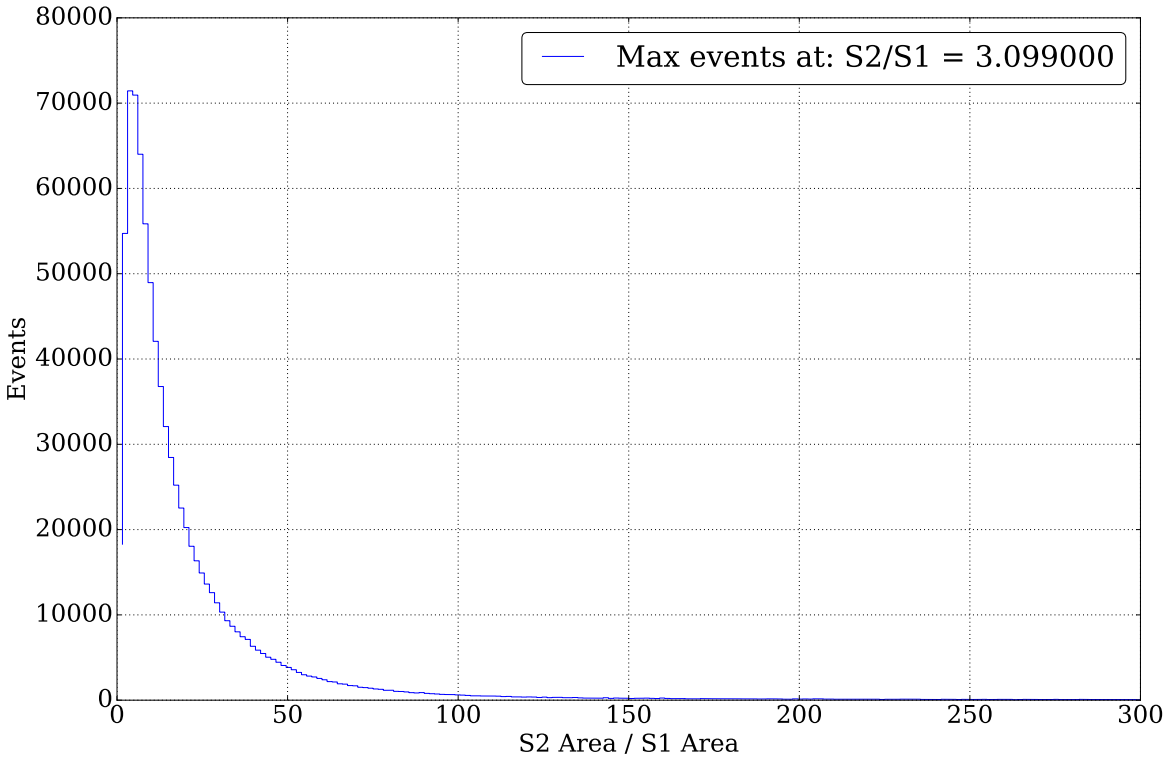

Figure 6.35: Histogram of the S2 Area S1 Area ratio for measurement 6.

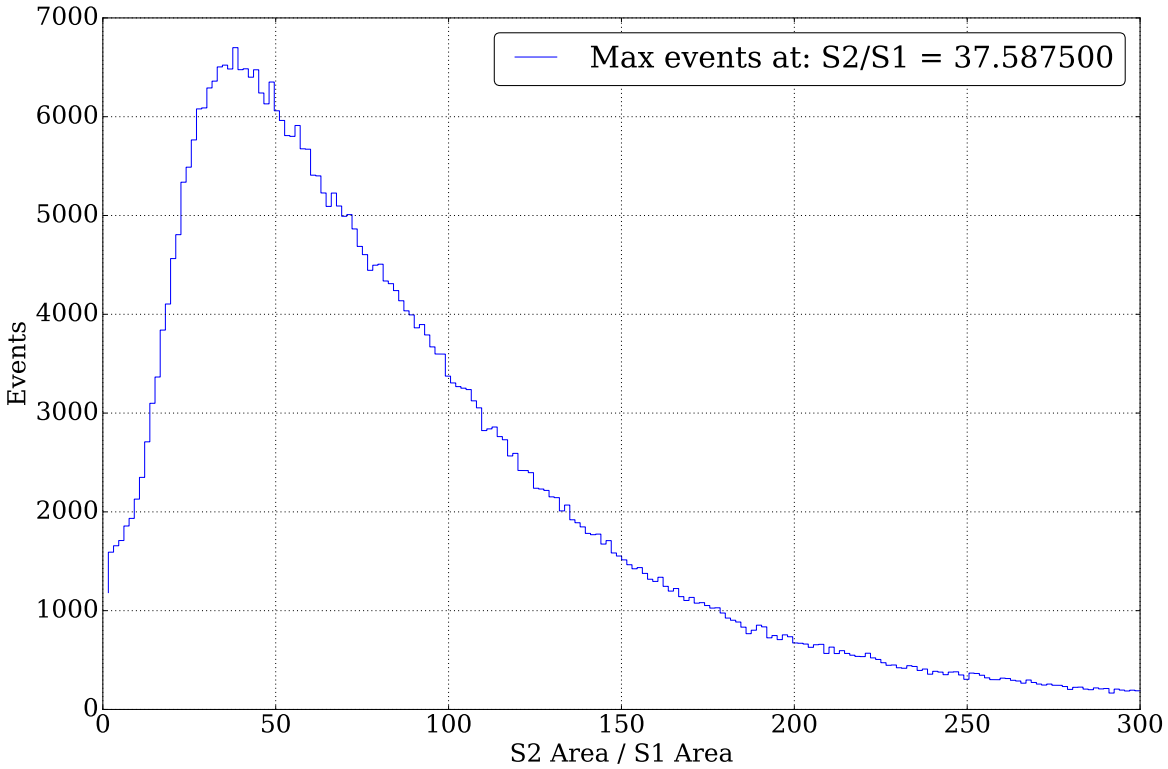

Figure 6.36: Histogram of the S2 Area S1 Area ratio for measurement 7.

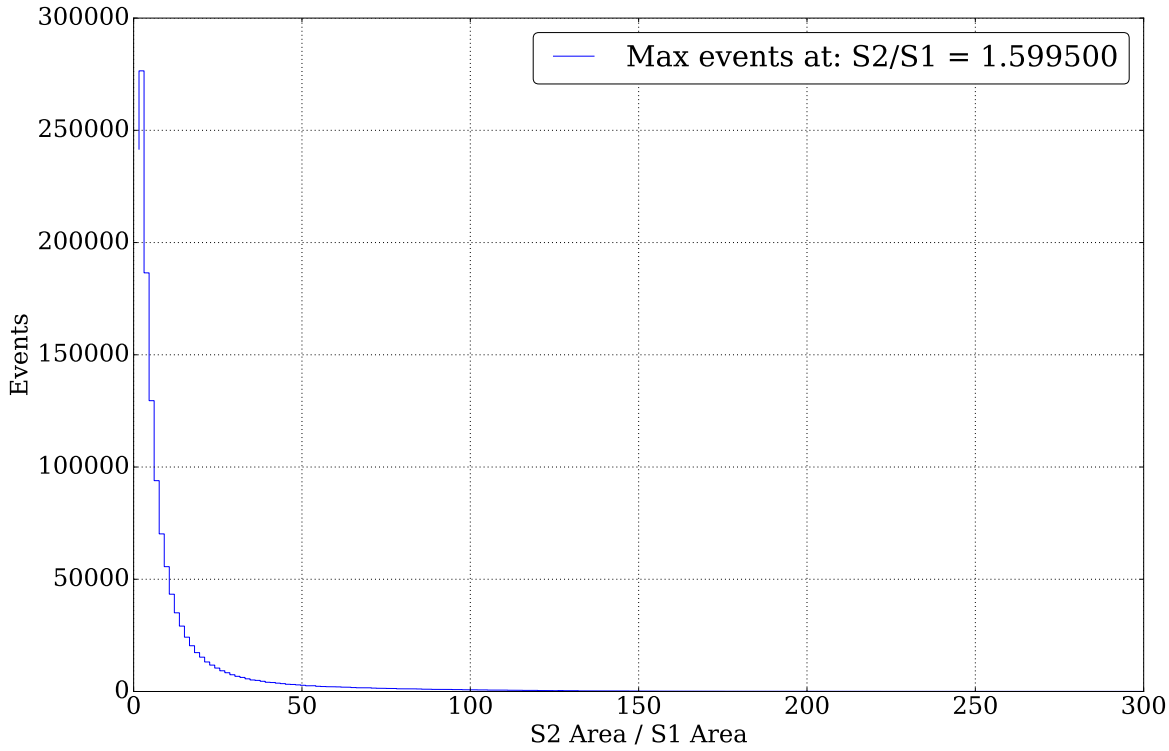

Figure 6.37: Histogram of the S2 Area S1 Area ratio for measurement 9.

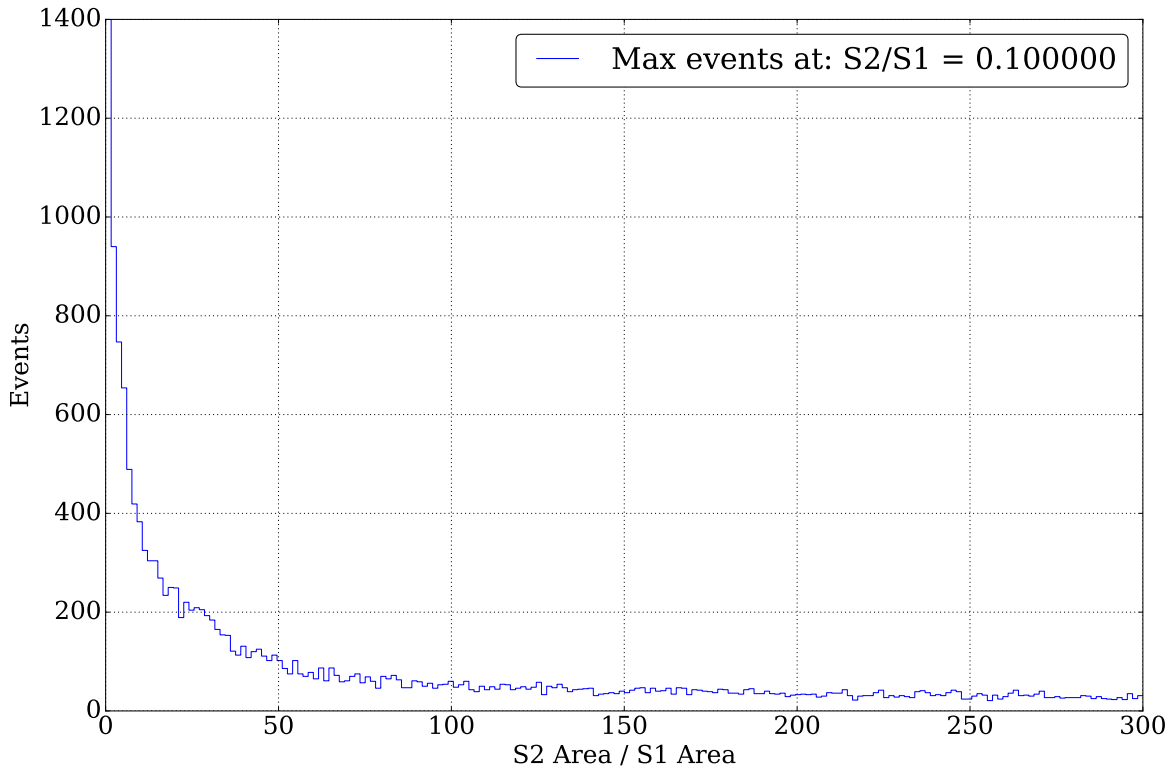

Figure 6.38: Histogram of the S2 Area S1 Area ratio for measurement 10.

Bibliography

[1] Elena Aprile et al. The xenon1t dark matter experiment. *arXiv preprint arXiv:1708.07051*, 2017. 3, 24

[2] Lutz Althüser. Geant4 simulations of the muenster dual phase xenon tpc. *Bachelor thesis*, September 2015. 4

[3] M Szydagis et al. Nest: a comprehensive model for scintillation yield in liquid xenon. *Journal of Instrumentation*, 6(10):P10002, 2011. 5

[4] E. Aprile and T. Doke. Liquid Xenon Detectors for Particle Physics and Astrophysics. *Rev. Mod. Phys.*, 82:2053–2097, 2010. 5

[5] Johannes Schulz. Design of a 2-phase xenon time projection chamber for electron drift length measurements. *Diplomarbeit*, December 2011. 5

[6] E. Aprile et al. The xenon100 dark matter experiment. *Astroparticle Physics*, 35(9):573 – 590, 2012. 6

[7] LS Miller, S Howe, and WE Spear. Charge transport in solid and liquid ar, kr, and xe. *Physical Review*, 166(3):871, 1968. 6

[8] LW Kastens, SB Cahn, A Manzur, and DN McKinsey. Calibration of a liquid xenon detector with kr 83 m. *Physical Review C*, 80(4):045809, 2009. 6

[9] Hamamatsu Photonics K.K. *Photomultiplier Tubes - Basics and Applications*, 3a edition, 2007. 7, 8

[10] Julian Blanke. Implementation of a fiberglass feed-through into the muenster time projection chamber for the calibration of the photomultipliers using a led pulser. *Bachelor thesis*, December 2015. 9

[11] P. Barrow et al. Qualification tests of the r11410-21 photomultiplier tubes for the xenon1t detector. *Journal of Instrumentation*, 12(01):P01024, 2017. 11

[12] The Scipy community. numpy.convolve, 06 2017. 13

[13] The Scipy community. scipy.optimize.curve_fit, 06 2017. 13

[14] Denny Schulte. Capacitance-based levelmeter read-out for the münster dual phase xenon time projection chamber. *Bachelor thesis*, 2016. 19, 20, 23

[15] Axel Buß. Characterization of the münster dual phase xenon tpc and of a newly developed magnetically driven piston pump. *Master thesis*, April 2016. 24